Optical and electronic properties of colloidal CdSe Quantum Rings

[1]James Xiao, [1]Yun Liu, [2]Violette Steinmetz, [1]Mustafa Çağlar, [1]Jeffrey Mc Hugh, [1]Tomi Baikie, [1]Nicolas Gauriot, [1]Malgorzata Nguyen, [1]Edoardo Ruggeri, [1]Zahra Andaji-Garmaroudi, [1,3]Samuel D. Stranks, [2]Laurent Legrand, [2]Thierry Barisien, [1]Richard H. Friend, [1]Neil C. Greenham, [1]Akshay Rao* and [1]Raj Pandya*

* correspondence: ar525@cam.ac.uk, rp558@cam.ac.uk

[1]Cavendish Laboratory, University of Cambridge, J.J. Thomson Avenue, CB3 0HE, Cambridge, United Kingdom

[2]Sorbonne Université CNRS-UMR 7588, Institut des NanoSciences de Paris, INSP, 4 place Jussieu, F-75005 Paris, France

[3]Department of Chemical Engineering & Biotechnology, University of Cambridge, Philippa Fawcett Drive, CB3 0AS, Cambridge, United Kingdom

Abstract

Luminescent colloidal CdSe nanorings are a new type of semiconductor structure that have attracted interest due to the potential for unique physics arising from their non-trivial toroidal shape. However, the exciton properties and dynamics of these materials with complex topology are not yet well understood. Here, we use a combination of femtosecond vibrational spectroscopy, temperature-resolved photoluminescence (PL), and single particle measurements to study these materials. We find that on transformation of CdSe nanoplatelets to nanorings, by perforating the center of platelets, the emission lifetime decreases and the emission spectrum broadens due to ensemble variations in the ring size and thickness. The reduced PL quantum yield of nanorings (~10%) compared to platelets (~30%) is attributed to an enhanced coupling between: (i) excitons and CdSe LO-phonons at 200 cm^{-1} and (ii) negatively charged selenium-rich traps which give nanorings a high surface charge (~-50 mV). Population of these weakly emissive trap sites dominates the emission properties with an increased trap emission at low temperatures relative to excitonic emission. Our results provide a detailed picture of the nature of excitons in nanorings and the influence of phonons and surface charge in explaining the broad shape of the PL spectrum and the origin of PL quantum yield losses. Furthermore, they suggest that the excitonic properties of nanorings are not solely a consequence of the toroidal shape but are also a result of traps introduced by puncturing the platelet center.

Introduction

The shape and size of a semiconducting nanocrystal is key to determining both its physical and optoelectronic properties *via* the nature of exciton quantum confinement[1]. Where spherical nanocrystals have 0D confinement, rod- and plate-shaped nanocrystals have 1D and 2D confinements leading to, for example, linearly polarized emission which is free of inhomogeneous broadening[2]. Over the last two decades, a remarkable degree of knowledge has been gained in synthesising these nanocrystals and their heterostructured variants (*e.g.* dot-in-plate)[3], with cadmium chalcogenide (CdX, X = S, Se, Te) materials finding particular use in a range of fields from catalysis[4,5] to neuronal voltage sensing[6].

Recently the shape of CdSe nanocrystals has been extended to nanorings by Fedin *et al.*[7]. Where dots, rods, *etc*. all belong to the topological class with genus (g) equal to zero ($g = 0$) and Euler characteristic $\chi = 2$, rings have $g = 1$ [8]. Due to synthetic challenges ring-like topologies are challenging to prepare. Epitaxial semiconductor rings have been shown to exhibit a range of unique properties including terahertz absorption and the formation of magnetoexcitonic quantum states (Aharonov-Bohm effect)[9,10]. Coupling these phenomena with a luminescent solution processable material would be highly desirable for a range of magneto-optical applications[11] *e.g.* data storage[12–14] or Faraday rotators[15].

Despite this, the electronic and optical properties of colloidal CdSe nanorings has remained largely unexplored, and although work by Hartmann *et al*[16]. has shown that excitons in rings possess an unusual arrangement of in-plane linear dipoles, the exciton dynamics have not been established. Here, we use a combination of ultrafast transient absorption spectroscopy and temperature-resolved optical and structural measurements to achieve an in-depth characterization of CdSe nanorings. Using absorption and TA measurements we establish that even a partial etch of the platelet induces a red-shift, a broadening of the absorption spectrum, and a decrease in the excited state lifetime. Density functional theory (DFT) calculations show that this is a result of changes in the electronic structure and overall material thickness in the direction of quantum confinement introduced by etching. The emission lifetime also decreases as the platelet is etched to form a ring, likely arising from the activation of phonon and trap mediated non-radiative decay pathways. Single particle PL measurements show the solution PL is inhomogenously broadened, likely arising from different sizes in the central hole from ring to ring, leading to non-uniform decay of the PL across the emission band and energy transfer between nanorings of different band energies. The emission quantum yield of the rings (~10%) is markedly lower than platelets (~30%). We find this to be a consequence of coupling between excitons, CdSe LO-phonons at 200 cm^{-1} and negative selenium rich traps. We quantify these charge effects with environmental Kelvin probe and zeta potential measurements. The structural modifications induced by etching of the platelet center systematically increase exciton-phonon coupling even when the platelet is only partially etched. Additionally, we find population of sub-band gap trap like states also governs the temperature resolved

emission of rings. We quantify the energy barrier for escaping from these traps to be ~8 meV, markedly lower than equivalent states in platelets (~21 meV). Finally, we qualitatively find that Auger and carrier cooling effects are less significant in rings than in platelets, with the excited state lifetime of the former independent of both excitation energy and intensity. We ascribe this to a hopping-type picture where excitations sit in sub-bandgap trap sites on the nanoring surface as compared to the delocalized band like picture of excitations in platelets. Our results provide a detailed description of excitons in a ring-like luminescent semiconductor, whose colloidal synthesis means its structure is drastically different from the "volcano-like" structures obtained using epitaxy[17,18]. These findings will be of use not only for realizing the potential of colloidal nanorings, but more generally in designing new topological semiconductors for optoelectronic and quantum technologies. By understanding in particular how defects deviate the properties of these materials away from ideality we will be able to better engineer the PLQY, lifetime, *etc*, for such applications.

Results and discussion

CdSe nanorings as shown in Figure 1a were synthesized using a method previously reported by Fedin *et al.*[7]. Briefly, 4-monolayer thick CdSe nanoplatelets were first synthesized , and showed an excitonic emission at 512 nm[2,19]. A solution of these nanoplatelets was then heated with Se powder for 5 – 10 min to etch the platelet center followed by quenching of the reaction with tributylphosphine. Further details of sample preparation and core/crown dimension analysis can be found in the Methods section. Unless otherwise stated all measurements were carried out in solution on rings with a hole dimension of ~5 - 10 nm. Samples were always measured within 3 days of preparation and stored and measured in an oxygen-free argon environment, to minimize oxidative degradation.

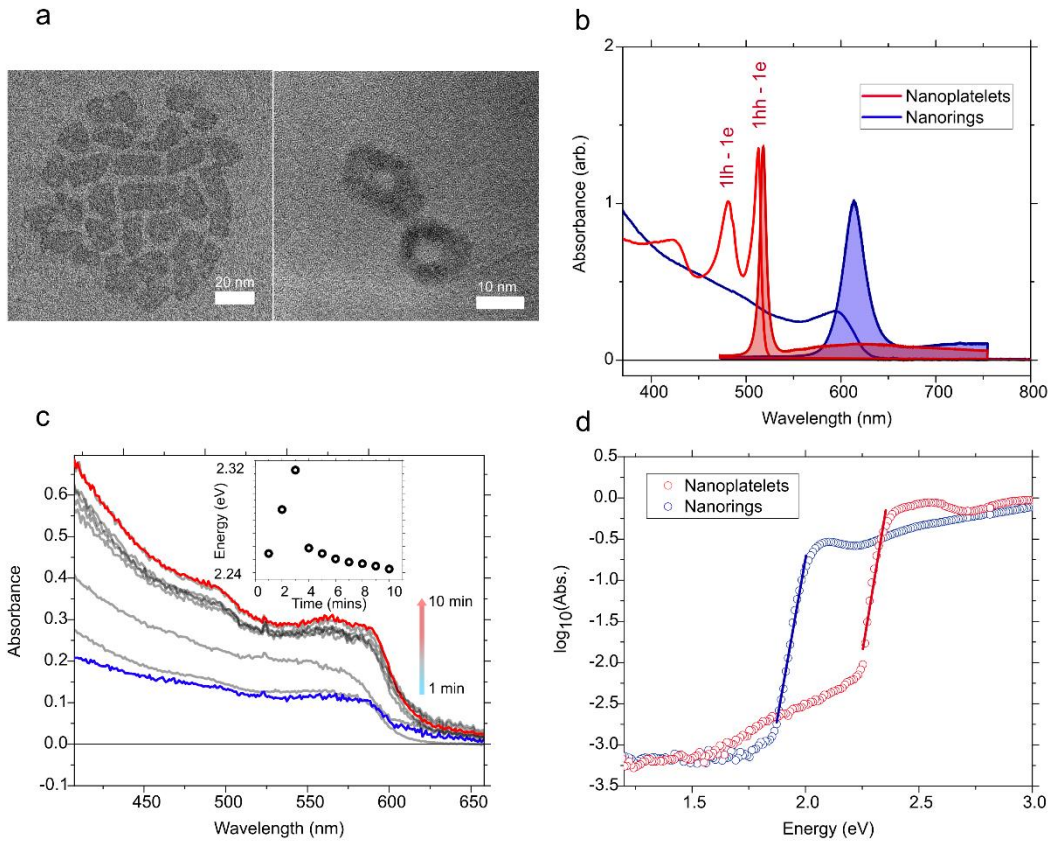

Figure 1: Structural and optical characterization of CdSe nanorings. a. Transmission electron microscopy (TEM) image of CdSe nanoplatelets (left) and nanorings (right). Nanorings are formed following etching of the nanoplatelet center. The scale bars in the two images are 20 nm and 10 nm respectively. **b.** Absorption spectrum of CdSe nanoplatelets (blue) and nanorings (red) in solution. Nanoplatelets show excitonic peaks at 512 nm and 482 nm corresponding to the electron-heavy hole and electron-light hole transitions. In nanorings there is a broad excitonic absorption centered at 600 nm. The respective emission spectrum for 405 nm laser excitation are shown in shading. **c.** Absorption spectrum of nanorings as a function of etch time. The nanoplatelet excitonic peaks disappear within the first minute of etching and are replaced by a broad absorption peak. The nanoring absorption edge (inset) red shifts over the etch time (10 mins) with the absorption growing in intensity. A second absorption peak emerges around ~470 nm when perforation is complete. TEM images (**SI, S1**) show that in 1 – 6 min the majority of nanorings remain partially etched (colour of spectra match arrow. **d.**

Photothermal deflection spectrum (PDS) of CdSe nanoplatelets (red) and nanorings (blue). Fitting the absorption tail, we find an Urbach energy of ~40 meV for nanoplatelets and ~38 meV for nanorings. In nanoplatelets there is a broad tail of absorbing states out to 1.5 eV these have been assigned to defects and inter-sub-band transitions[20].

To understand better the transformation of nanoplatelets to nanorings *in situ* absorption measurements were performed. Here, aliquots of solution were taken at given times during etching. Figure 1b, c shows the absorption spectra for 4-monolayer (ML) nanoplatelets and nanorings in solution. In order to minimize the effects of scattering, measurements were carried out within an integrating sphere (see Methods). In contrast to the sharp absorption and weakly Stokes shifted emission of nanoplatelets, nanorings show a broad absorption with an emission that is red-shifted from the absorption peak. Immediately (within 1 min) after reaching reaction temperature it can be seen that the sharp CdSe 1lh-1e and 1hh-1e excitonic transitions[19] disappear and are replaced with a broad absorption feature that gradually red shifts as a function of etch time (although we note that the predominant optical changes take place below our time resolution, within 1 min of etching). This additional red-shift is most likely a consequence of the increased thickness of the rings over that of the initial platelets. This will in turn alter the nature of quantum confinement and mitigate any blue-shift that would be expected from the extra confinement conditions introduced by having excitations on a ring. An additional absorption feature around 500 nm also grows in throughout the etching process. Because there is a range of ring thicknesses (along the long and short-axes of the ring) and variation in the inner and outer ring diameters, following addition of the etchant, the absorption peak is broad and more closely resembles that observed in 0D dots[1]. Structural measurements performed in the initial work of Fedin *et al.* additionally confirm increase in thickness on transforming platelets to rings[16]. We note that the TEM image of nanorings in Figure 1a show some variation in contrast suggesting the thickness of individual rings is non-uniform. Although this will increase the electronic disorder of nanorings, it does not appear to lead to multiple *emissive* excitonic sites as demonstrated by single particle PL measurements (see later).

To understand this change in the absorption spectra further, we performed DFT calculations. We used a nanoplatelet infinite in lateral dimensions and 2 CdSe monolayers thick to represent the pseudo-2D nanoplatelet synthesized in experiments, which possess lateral dimensions much larger than the Bohr exciton radius (~5.4 nm)[21]. The top and bottom {100} surfaces of the platelet were passivated with chloride ligands to ensure overall stoichiometry[22,23]. The nanorings were created by removing atoms from the platelets to form holes of different sizes. Further details about the DFT calculations can be found in the Methods. As seen in Figure 2a, the platelet exhibits the two absorption peaks due to the 1lh-1e and 1hh-1e. These peaks are red-shifted compared to experiments due to the well-known underestimation of the semiconductor bandgap by DFT. Compared to the platelet, the first absorption peaks of the nanorings are red shifted by about 150-300 meV, in qualitative agreement with

experiments. Although we note this peak has low a relatively low intensity and because exciton effects are not included in our calculations likely only gives a qualitative picture. As indicated by Figure 2b, when a small ring is initially formed, a set of localized states (Figure 2c) emerge just above the valence band maximum (VBM). These states are mainly of Cl characteristics (**SI, S2i**) and are localized on opposite sides of the ring. The wavefunction localization pattern is consistent with the *k*-vector resolved PL emission reported by Hartmann *et al*, whereby the measured radiation pattern shows bright lobes on opposite ends of the ring.[16] The change in topology only affects the VB states, and the conduction band states near the Fermi level remain delocalized and energetically similar to those of the nanoplatelet (**SI, S2ii**). We do note that our calculation is for the stoichiometric nanoring structure whereby all dangling bonds were passivated, but in experiments the existence of dangling bonds could introduce additional trap states and changes in the electronic structure[24,25].

Our DFT results suggest that the energy shifts in the experimental absorption spectra likely arises from two effects: (i) the redshift in the absorption peak as more materials are pushed onto the rings as the etching proceeds, increasing the thickness in the quantum confinement direction and (ii) the blueshift in the absorption peak as the size of the ring increases.

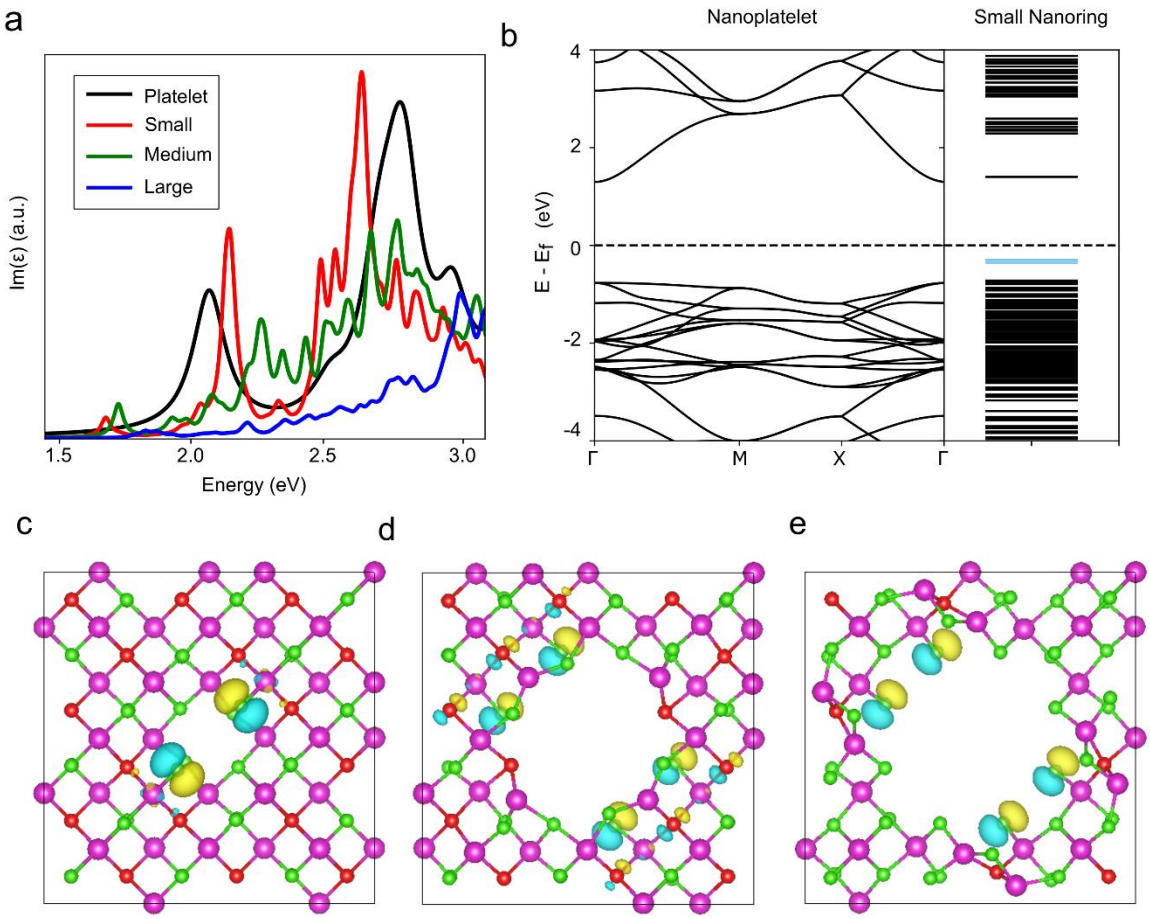

Figure 2: DFT calculations of nanoplatelet and nanoring. a. In-plane absorption spectra (imaginary part of the dielectric function) of the nanoplatelet compared with nanorings of different sizes. **b.** The bandstructure of the CdSe nanoplatelet, with the Fermi level denoted by the dashed line. The special *k*-points in the Brillouin zone of the reciprocal lattice are Γ = {0,0,0}, M= {0.5,0.5,0.5} and X = {0.5, 0.0, 0.0}. The band energies at the Γ point of the small nanoring compared to the nanoplatelet. The localized states at the top of the VBM are highlighted in blue. **c- e.** The in-plane view of the ball-and-stick model of the nanorings of small, medium and large sizes respectively. The Cd, Se and Cl atoms are represented by magenta, red and green spheres. The isosurfaces of the VBM wavefunction are colored cyan and yellow. The data are visualized using VESTA[26].

To understand the role of disorder introduced by etching of the platelet center were performed using photothermal deflection spectroscopy (PDS), which is insensitive to scattering (Figure 1d; Methods)[27]. The PDS absorption spectra of rings shows a single excitonic peak at ~2 eV followed by a relatively sharp drop. For platelets a similarly sharp drop in the absorption is observed around 2.25 eV but this levels to a weak and broad absorption feature around 2 eV likely related to the absorption of sub-gap or defect states[20,28,29]. Having identified the relevant tail transitions, we can use the PDS measurements to quantify the energetic disorder of both rings and nanoplatelets. This is characterized by the Urbach energy, E_u, which is related to the absorbance of the material, A, by $A(E) \propto e^{\frac{E}{E_u}}$, where E is the photon energy[30]. Fitting the absorption tail in Figure 1d to the Urbach formula gives an E_u value of 40 ± 1 meV for CdSe platelets and 38 ± 1 meV for CdSe nanorings. This value is approximately 4 times larger than that obtained for high-quality GaAs, but lower than values obtained for CdS and CdSe/CdS nanocrystals ($E_u \approx$ 48–65 meV)[31,32] and common organic semiconductors (P3HT ≈ 50 meV)[33]. This suggests that although there is a change in the electronic structure on etching of nanoplatelets (with potential thickness variations within a single ring) these changes do not significantly impact the degree of electronic disorder. This is likely because the surfaces/edges of the nanostructures, common to both, is where most of the traps contributing to the Urbach energy are located. We note in nanoplatelets there is an additional tail of absorbing states between 1.5 – 2 eV, which may arise from surface defects or sub-band gap states.

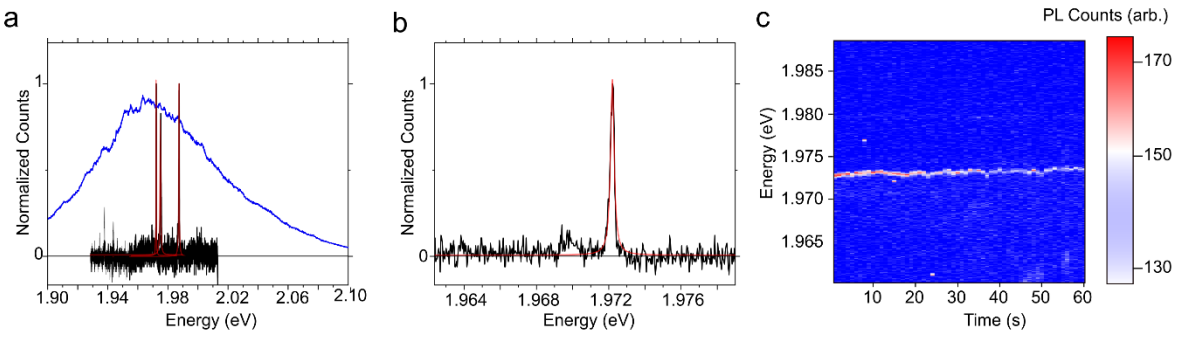

Figure 3: Photoluminescence spectra of single CdSe nanorings at 4 K. a. Typical emission spectra of single CdSe nanorings (black lines; each of the spectra is taken from a *different* single object). Red overlay shows a Lorentzian fit to the spectra, with blue spectrum indicating photoluminescence from ensemble. A range of emission energies are observed for single nanorings suggesting the ensemble spectrum to be composed of rings of varying thickness and/or diameter. **b.** Zooming into an example single nanoring PL spectrum shows a line width of ~250 μeV in FWHM. **c.** Time-dependent spectrum of emission from a single nanoring. The emission intensity decreases as a result of photobleaching, with no new peaks growing in and relatively little peak shifting.

The photoluminescence spectrum of nanorings in solution is relatively broad (FWHM ~90 meV) compared to nanoplatelets (FWHM ~ 35 meV). To understand whether this originates from sub-structure within the emission spectrum or inhomogeneous broadening effects, low-temperature (4 K) single-particle PL measurements were performed. There is no phase change in the structure of either nanoplatelets or nanorings on cooling to 4 K (**SI, S3**). As exemplified in Figure 3a-b single nanorings show a single sharp emission peak varying in center frequency between 1.94 and 2.00 eV and 250 – 700 μeV FWHM in width. This behavior is in contrast to nanoplatelets where uniform quantum confinement leads to an unchanging linewidth between the ensemble and single particles, with single-particle linewidths ~400 μeV[34]. Based on our DFT calculations nanorings with a larger radius are expected to have a larger bandgap and contribute to the higher energy emission within the ensemble, with smaller rings showing red-shifted emission, potentially explaining the observed variation in emission energies. Alternatively, the distribution in nanoring bandgaps may arise from variations in thickness between rings induced during the etching process, with thicker rings having more red-shifted emission. We note that the observation of a single emission peak in the single-particle spectra suggests any variation in thickness still only leads to a single emissive site. In any case, the narrow single-particle line widths suggest that nanorings have potential for optical applications such as single photon sources, where the emission can be coupled with the unusual radiation pattern (Hartmann *et al*.[16] showed the transition dipole moments in CdSe nanorings are arranged in a uniaxial, in-plane manner) arising from the annular shape[16]. It is challenging to quantitatively determine the distribution in ring sizes in the ensemble, however dynamic light scattering (**SI, S9**) measurements can be used to qualitatively estimate this. Here we find an average (total) nanoring size (hydrodynamic radius) of 15.2 ± 1.4 nm, implying a ~10% variation in the ring size. This variation in sizes combined with any variations in the confinement in the transverse direction of the rings (thickness) likely contributes to the variation in emission energies observed.

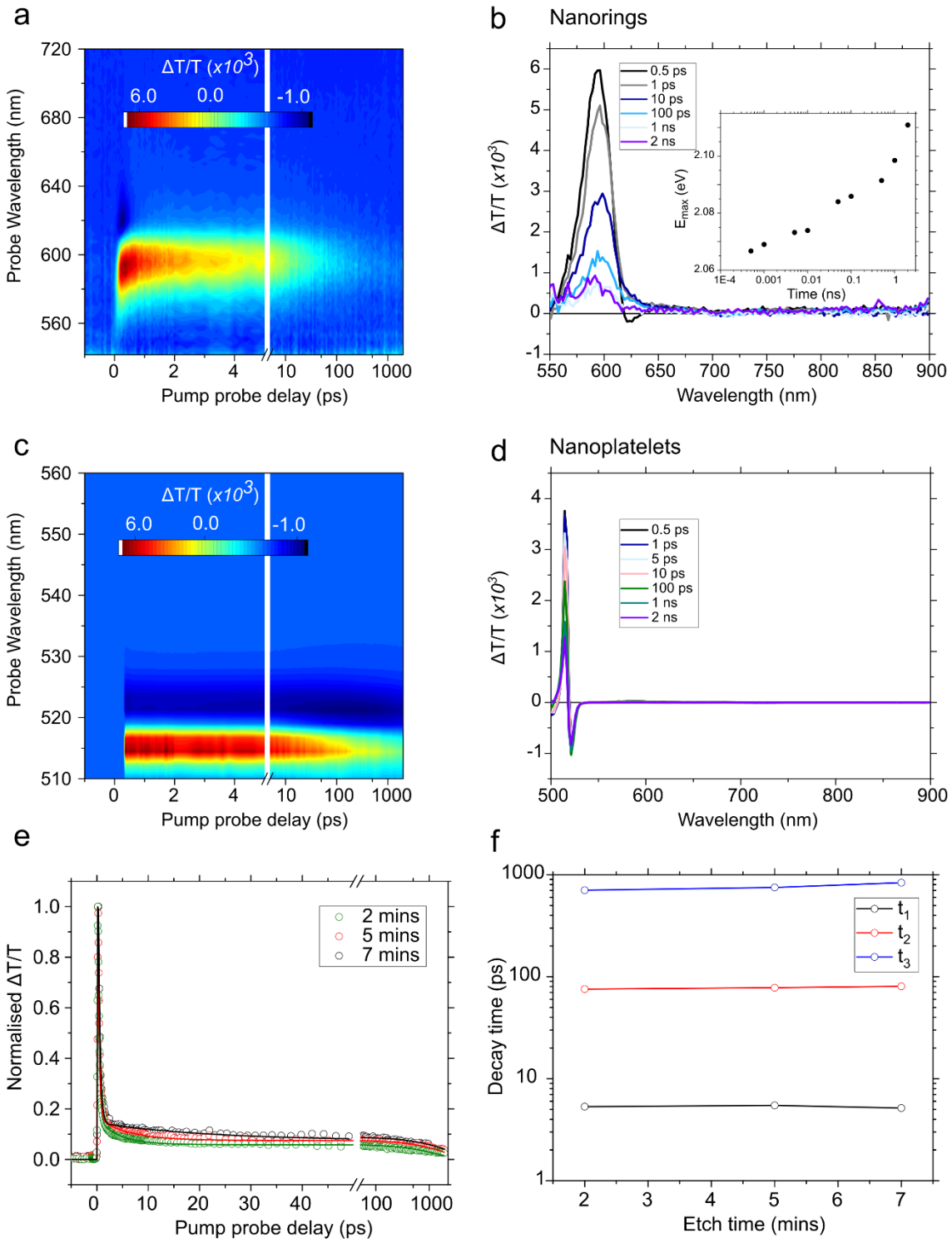

Figure 4: Transient absorption spectrum of nanoplatelets and nanorings following photoexcitation with a sub-10 fs pulse. a. Transient absorption spectrum of nanorings. There is a gradual red-shift (~50 meV; see inset) and narrowing of the bleach peak following photoexcitation which is ascribed to hopping of excitations between defect sites and to nanorings with the lowest bandgap within the ensemble. **b.** Selected spectral slices at given time delays of transient absorption spectrum of nanorings. The weakly pronounced negative wing around ~625 nm, which is typically assigned to Stark shifts in nanocrystals[35], suggests that exciton-exciton interactions are relatively weak

in nanorings. **c.** Transient absorption spectrum of nanoplatelets. Following photoexcitation there is relatively little shift in the excitonic peak, with a significantly slower, multi-exponential decay as compared to nanorings. **d.** Selected spectral slices at given time delays of transient absorption spectrum of nanorings. The GSB is relatively long-lived as compared to in nanorings. **e.** Decay rate of the ground state bleach of nanorings as a function of etch time. **f.** The first and second decay constants (t_1 and t_2) do not change significantly with etch time. The final decay constant (t_3) appears to slightly lengthen as the platelet center is further etched.

Although several studies have addressed the steady-state properties of CdSe nanorings, no experiments have been able to elucidate how the exciton *dynamics* are influenced by their toroidal structure[7,15]. In order to directly probe the exciton dynamics in nanorings and understand how these excitons interact with phonon modes, we conducted femtosecond transient absorption (fs-TA) spectroscopy. A solution of nanorings was excited with a 9 fs pump pulse (upper limit verified by second-harmonic-generation frequency-resolved optical gating[35] (SHG-FROG); **SI, S4**) centered at 530 nm such that it was partially resonant with the exciton transitions of the rings. Figure 4a shows the transient absorption spectrum of nanorings, where $\Delta T/T$ is plotted as a function of probe wavelength and time delay between pump and probe. ΔT is the change in the transmission of the sample with/without the pump pulse, and T is the transmission without the pump pulse.

The positive narrow signal centered at around 580 nm (Figure 4a,b) corresponds to the ground-state bleach (GSB) of nanorings, which agrees well with the steady-state absorption (Figure 1b; we note at the fluences used here there are ~0.15 excitations per nanorings; see **SI, S5**). This GSB decays with two lifetimes, an initial fast component of ~2 ps, followed by a much slower decay with a ~30 ps lifetime. The bleach red-shifts over a period of ~10 ps before beginning to decay (see Figure 4b inset). On the lower-energy edge of the bleach there is a weak negative feature. In nanoplatelets (Figure 4c,d) the transient absorption response is quite different. Here there is a relatively slow tri-exponential decay of the bleaching peak with an average decay time of ~920 ps and little-to-no-peak shifting following excitation (fit **SI, S5**). There is also a strong negative band on the red-edge of the GSB.

Several groups have performed and analyzed the transient absorption spectra of CdSe nanoplatelets. The derivative-like spectrum can be explained well by a model that accounts for state-filling-induced bleach of the electron-heavy hole and electron-light hole exciton transitions, a Stark shift in the center frequency of these transitions due exciton-exciton interactions and bandgap renormalization[36–39]. Hole-trapping at surface defects and delocalization of excitons over the nanoplatelet have also been stated to occur in the first ~100 ps following photoexcitation in these materials[40]. This potentially explains why the GSB at 512 nm is comparatively short-lived compared to the negative feature at 525 nm, with state filling at the band edge replaced by trap state absorption and a large Stark shifts induced by more delocalised electrons at a band edge level (see **SI, S5**).

In nanorings there is a much weaker derivative-like shape to the spectrum with the negative wing on the red low-energy edge of the GSB decaying rapidly over ~1 ps. The spectrum is strongly reminiscent of that observed in metal halide perovskites, where following photoexcitation there is rapid (sub-500 fs) renormalization of the bandgap, giving rise to an early-time derivative feature, followed by cooling and hopping of excitations to localization sites[41–43]. The lack of persistence of this negative wing suggests that hot carrier induced exciton-exciton interactions are also weaker in nanorings in keeping with a picture of localized excitations[44,45]. This conclusion is supported by experiments on partially etched platelets, where the initial fast decay time remains independent of etch time, but the slow component lengthens, potentially as a result of more sub-bandgap trap states being introduced as the etch progresses (Figure 4e,f). This lack of negative feature in the transient absorption spectrum of nanorings compared to nanoplatelets also suggests a smaller biexciton binding energy in these materials. This is in line with the increased thickness of nanorings compared to nanoplatelets where Coulomb interactions are screened by the inorganic material.

Given the significant inhomogeneous broadening in the emission of nanorings, the red-shift (~50 meV) in the center frequency of the GSB over ~1 ps, may also represent energy transfer to the lowest energy nanorings within the solution ensemble with different recombination rates within the manifold[46,47]. However, the relatively large (~90 meV) Stokes shift between the absorption and emission of nanorings suggests that this may only be a partial effect. Indeed, performing pump-probe measurements as a function of ring concentration shows minimal change in the degree of red-shift (~35 meV in dilute solutions) suggesting that energy transfer does not play a dominant role (see **SI, S5** for further discussion and FRET calculations which show a FRET efficiency <2%).

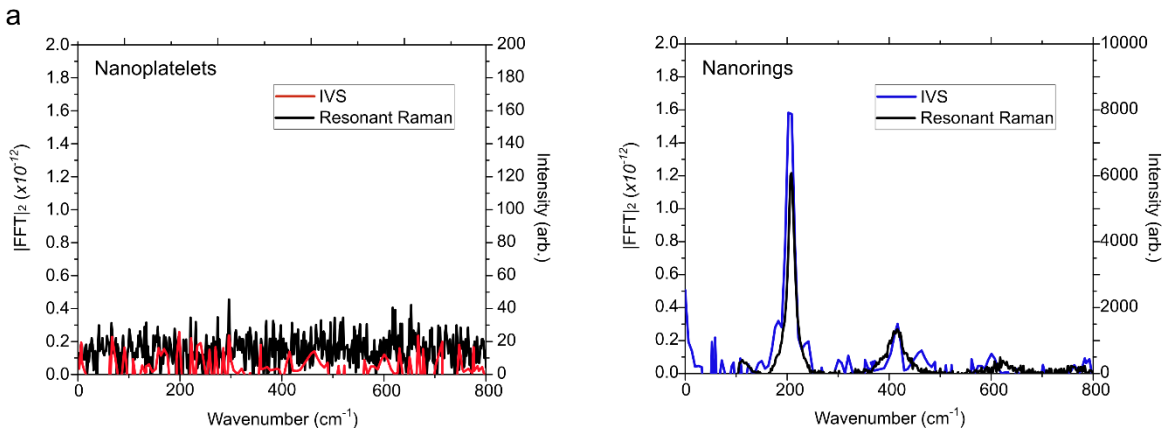

Figure 5: Impulsive vibrational spectrum and resonant Raman spectra of nanorings and nanoplatelets. a. Subtracting the electronic decay from the nanoring bleach and Fourier transforming the residual gives the impulsive (state-specific) vibrational spectrum (blue). Two clear peaks are observed at 200 cm^{-1} and 400 cm^{-1} corresponding to the CdSe LO-phonon stretch and its replica. These peaks also appear in the resonant (532 nm) Raman spectra (black). **b.** Repeating the same analysis for nanoplatelets appears to show no modes in either the IVS or Raman spectra, suggesting weak exciton-phonon coupling.

As the samples are excited with a sub-10 fs pump pulse, vibrational wavepackets can be generated on both the ground- and excited-state potential energy surfaces[48–50]. These then appear as an oscillatory feature on top of the electronic decay, as seen in the TA map and kinetics[51]. In order to extract the frequency of the vibrational modes, the electronic component of the TA spectrum in Figure 5a and b was subtracted and the remaining oscillatory component fast Fourier transformed into the frequency domain (see **SI, S6**). In the case of nanorings a single mode centered at ~200 cm^{-1} (frequency resolution 16 cm^{-1}; dephasing time ~800 fs) is observed to modulate the GSB, whereas in nanoplatelets no modes are seen to modulate the spectra (Figure 5). Performing steady-state resonant (532 nm) and off-resonant (633 nm) Raman measurements also shows the 200 cm^{-1} mode to be present in nanorings but there are no observable modes in the Raman spectra of nanoplatelets, consistent with previous studies where only weak-exciton phonon coupling has been observed[52]. Analyzing the literature shows this 200 cm^{-1} mode corresponds to an LO-phonon of CdSe[53–55]; this mode also appears in the steady state and time domain Raman spectra of partially etched nanorings confirming it to be introduced by the etch, but is likely not necessarily a consequence of the annular shape (**SI, S7**). Strong coupling of excitons with this phonon mode further supports the idea of rapid localization of excitons in nanorings following photoexcitation. This is in contrast to the picture of excitons in nanoplatelets where the greater delocalization likely leads to weaker exciton-phonon coupling[52,56–59]. Based on our DFT calculations, the strong localization of the excitons in the nanorings can be attributed to some degree to strong localization of the hole states that emerged in the nanoring electronic structure.

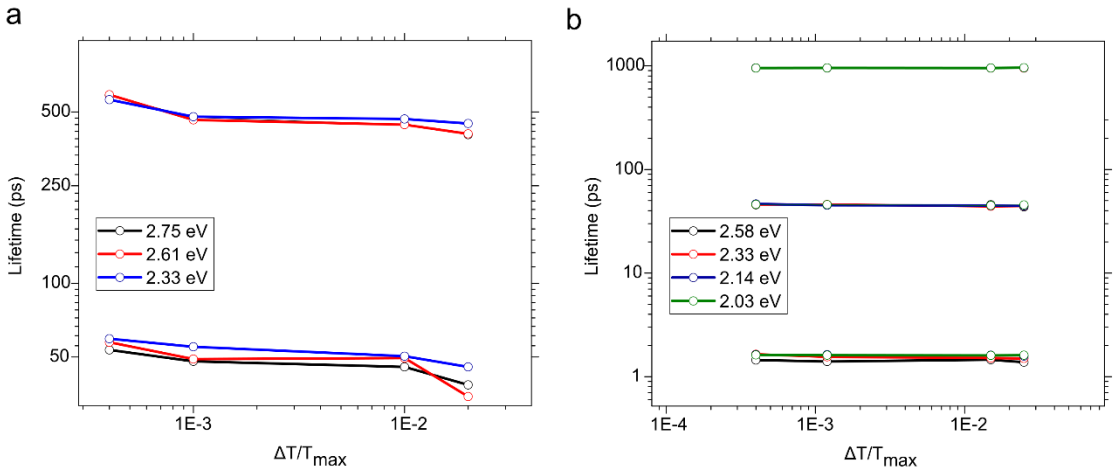

Figure 6: Pump energy and intensity dependence of transient absorption dynamics in nanoplatelets and nanorings. a. In both nanoplatelets and nanorings the ground state bleach shows a multi-exponential decay. For nanoplatelets pumping at higher energies away from the band edge and with higher pump intensities results in faster decay components. This is suggestive of cooling and Auger recombination within a band like picture of excitations. **b.** In nanorings there is no pump energy or intensity dependence in the dynamics (in the excitation regime studied here where there is less than 1 excitation per particle; see **SI, S5** for fluence dependence and carrier concentration calculations). In

both panels the error on the fitted decay is sufficiently small (± 10 ps) that is not shown so as to maintain clarity.

Using a narrow-band excitation pulse (FWHM ~10 nm, pulse duration ~200 fs), we can also study the excitation energy and laser intensity dependence of transitions in both rings and platelets (Figure 6; we note that for each measurement a similar carrier concentration is maintained between nanoplatelets and nanorings (see **SI, S5**)). In the case of nanoplatelets on increasing both the pump fluence and energy there is a qualitative shortening of the GSB lifetime (Figure 6a). This is in keeping with a model of state filling within a valence band where the cooling time decreases when pumping closer to the band edge and Auger recombination increases with greater excitation densities[60,61]. In contrast, nanorings do not appear to show any pump energy or excitation density dependence in their transient absorption response. This would again fit with a trap-like picture where excitons hop from site-to-site before localizing, likely assisted by the 200 cm^{-1} phonon mode, as opposed to being delocalized in band states. Regardless of pump energy and intensity, in both nanorings and nanoplatelets cooling times remain on the sub-picosecond timescale, suggesting as in 0D CdSe QDs the phonon bottleneck is bypassed *e.g.* by transfer of energy from hot electrons to holes[62]. In nanorings, our results suggest that any excess energy is also rapidly dissipated before any localization occurs.

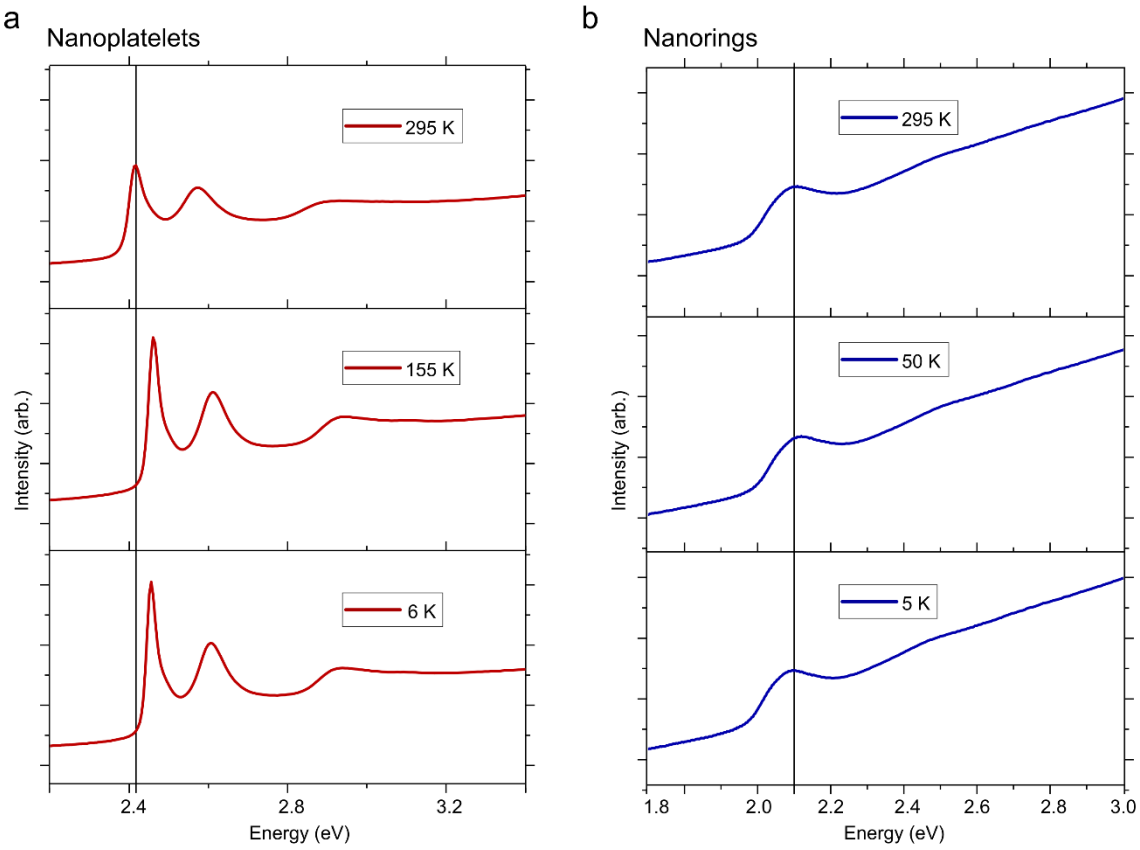

Figure 7: Temperature dependent absorption spectra of nanoplatelets and nanorings. a. The absorption spectra of nanoplatelets (red) initially blue-shifts to higher energies on cooling, followed by a gradual red-shift when cooling below 20 K. Solid line marks absorption maximum at 295 K. **b.** In nanorings (blue) there is a similar blue- and then red-shift in the absorption maximum on cooling. Temperature X-ray diffraction measurements confirm there is no phase transition on cooling for either nanorings or nanoplatelets (see **SI, S3**).

Figure 7 reports temperature dependent absorption measurements for films of nanoplatelets and nanorings. In the case of both nanorings and nanoplatelets the absorption spectrum initially shows a concomitant blue-shift to higher energies on cooling. In both materials the absorption spectrum then begins to red-shift to lower energies below a certain temperature (~60 K in nanoplatelets and ~100 K in nanorings). In nanoplatelets this effect has been previously ascribed to phonon-mediated thermal redistribution between two levels having different oscillator strengths (**SI, S8**)[63]. Given the similar behaviour we can hence tentatively suggest in this regard a similar two electronic state picture potentially exists for excitons in nanorings. Here, when the thermal energy becomes smaller than any energy splitting, only the lower level will be thermally populated. However, at elevated temperatures both upper and lower states are populated and because the upper state has a higher oscillator strength, this state will dominate the optical behaviour.

In nanoplatelets a similar behaviour as to that discussed above is also realised in emission measurements, with a non-monotonic change in the PL intensity and wavelength with temperature and a red-shifting zero-phonon line below 80 K (Figure 8a). A second weakly emissive state also appears centered around 630 nm in nanoplatelets. We note this state is unlikely to arise from a population of thicker nanoplatelets, as the thickest stable CdSe nanoplatelets synthesised thus far (6 monolayers) have their emission centered around ~590 nm[64]. For the case of nanorings the temperature resolved emission shows some similarities to nanoplatelets but also some differences. In these materials the PL intensity is rapidly reduced on decreasing the temperature with a second spectrally broad (~70 meV at 4 K) emissive state (centered around 660 - 740 nm) growing in intensity on cooling. The difference in energy between trap states in nanoplatelets and nanorings suggests that although they are both likely located in a similar location *i.e.* at the surface, the change in electronic structure arising from shape nanocrystal shape alters their energies. At 5 K the main excitonic emission and emission from this second state are almost equal in intensity, in contrast to the nanoplatelets where emission from the excitonic state is ~10 times greater than emission from the state at ~630 nm, even at 4 K. We assign these observations to population competition with low-lying trap states as has been observed in 0D quantum dots[65,66]. At low temperatures excitations localize in these trap states from which some fraction of the excitons can decay radiatively. The PL intensity of the band-edge (BE) emissive state and trap state will be proportional to the occupation, n, which follows a Boltzmann distribution, giving:

$$\frac{PL_{BE}}{PL_{trap}} \propto \frac{n_{BE}}{n_{trap}} = \frac{g_{BE}}{g_{trap}} e^{\left(\frac{-\Delta E}{kT}\right)} \quad \text{(Equation 1)}$$

In this equation ΔE is the energy difference between traps and the band-edge excitonic state and g_{BE} and g_{trap} are the band edge exciton and trap state degeneracy respectively. Fitting the PL ratio intensities from these two states as shown in Figure 6 for nanoplatelets and nanorings then allows us to determine the trap-state depth. In this fitting we make the assumption that any charge transfer is sufficiently fast to establish an equilibrium between traps and band-edge states and consequently only perform the fit at high temperatures (T>200 K)[67]. Fitting the data yields trap activation energies of 21 ± 5 meV for nanoplatelets and 8 ± 5 meV in nanorings. We note these are both consistent with the observation of room temperature emission from trap states. One final observation from these low temperature PL measurements is that the PL maximum initially slightly blue-shifts and then begins to red-shift below 150 K in nanorings, suggesting the main emission from the main excitonic state is still consistent with a model similar to that observed in nanoplatelets (Figure 8c and e).

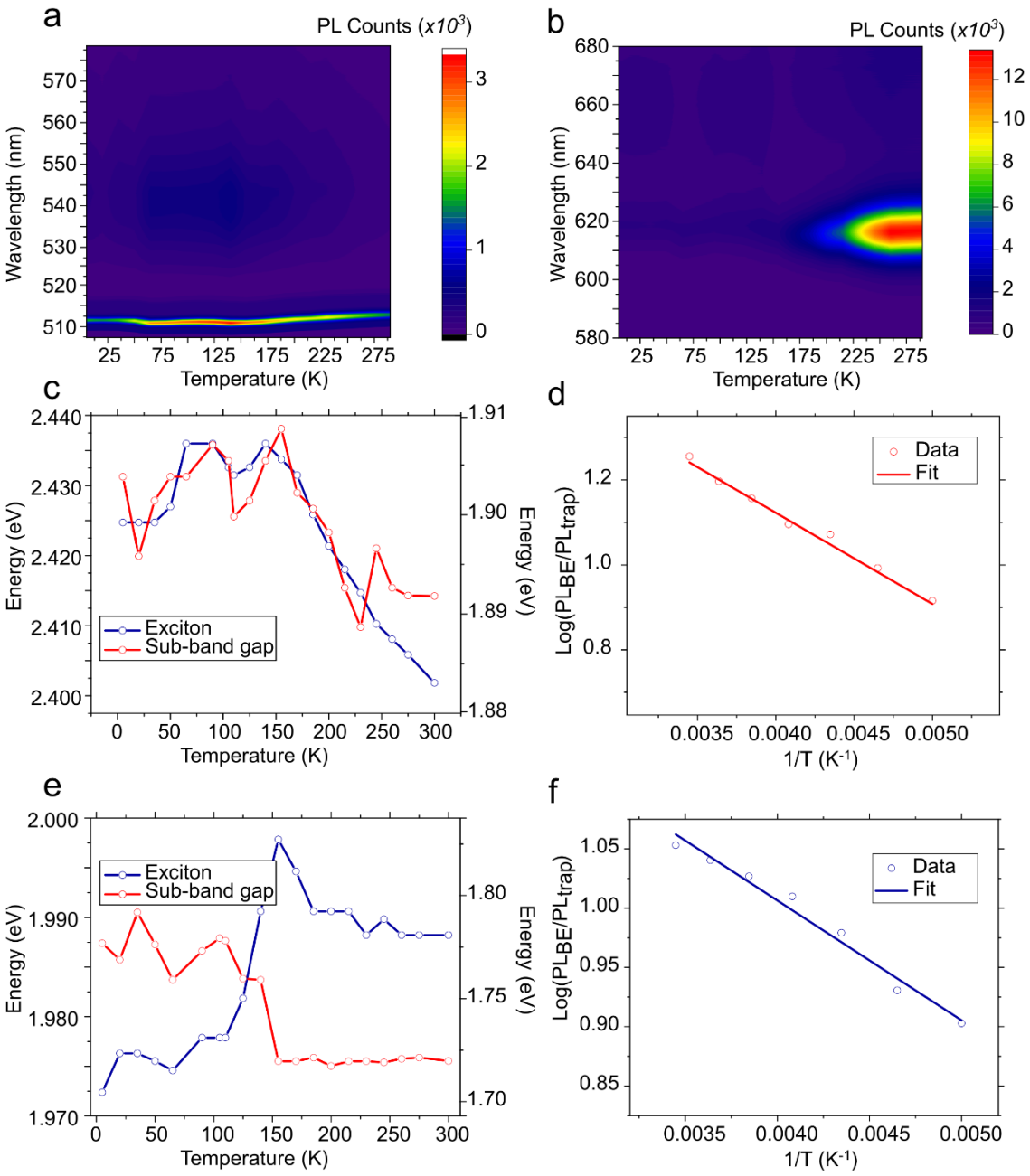

Figure 8: Low temperature emission spectra of CdSe nanoplatelets and nanorings. a. Emission spectra of CdSe nanoplatelets excited at 405 nm. A non-monotonic change in the PL intensity and maximum peak position is observed on cooling, with some secondary sub-band gap emission centered around 660 nm (see **SI, S8** for spectral slices). **b.** Emission spectra of CdSe nanorings. As for nanoplatelets, the excitonic emission initially blue-shifts to higher energies on cooling before red-shifting when below 100 K. There is a secondary sub-band gap emission peak which grows in intensity on cooling. There is a secondary sub-band gap emission peak which grows in intensity on cooling. **c.** Maximum peak position for excitonic and sub-band gap emission as a function of temperature for CdSe nanoplatelets. The maximum peak position for both the sub-band gap and excitonic state in

nanoplatelets initially shows a red-shift followed by a blue-shift below 100 K. **d.** Log of ratio of integrated intensities for excitonic and sub-band gap emission in nanoplatelets. At room temperature there is ~16 times more emission from the excitonic state as compared to sub-band gap emission. At low temperature this ratio is reduced to ~8 (**SI, S8**). Fitting the high temperature data (T > 200 K) with the model in equation 1 allows extraction of the trap activation energy of ~21 meV. **e.** Maximum peak position for excitonic and sub-band gap emission as a function of temperature for CdSe nanorings. Where the sub-band gap emission only blue-shifts to higher energies on cooling, the excitonic emission in nanorings initially shows a red-shift followed by a blue-shift. **f.** Log of ratio of integrated intensities for excitonic and sub-band gap emission in nanorings (PL_{BE}/PL_{trap}). At room temperature there is ~11 times more emission from the excitonic state as compared to sub-band gap emission, whereas at low temperature the emission intensity from these two states is almost equal (**SI, S8)**. Fitting the high temperature data (T > 200 K) with the model in equation 1 allows extraction of the trap activation energy of ~8 meV.

In order to understand the loss of emission towards trap states in nanorings and nanoplatelets transient photoluminescence measurements were performed (Figure 9) on solutions of nanorings and nanoplatelets. In both nanoplatelets and nanorings a multi-exponential decay is observed. In nanoplatelets the initial fast component of the decay (>10 ns) has been ascribed to cooling, energy transfer and Auger decay which are accelerated due to a 'giant oscillator strength' effect[2]. The delayed component of the emission (which has been shown to extend to beyond 20 μs) has been assigned to reversible charge trapping/detrapping. The emission decay in platelets is uniform across the band in keeping with the low-inhomogeneous broadening and a picture of delocalized excitations. By contrast the PL decay in nanorings is much shorter than platelets, although also multi-exponential, with the decay here well described with three decay constants of 1.3 ± 0.2 ns, 7.2 ± 2 ns and 40.3 ± 2 ns. The absence of a long-lived emission component in the decay suggests a model using reversible-carrier trapping/delayed luminescence cannot be used to explain the PL decay in these materials[68]. In light of the aforementioned evidence for localization of excitations in nanorings, the fast component of the PL decay is potentially associated with a combination of cooling processes and energy transfer between different nanorings within the inhomogeneously broadened PL. The slower part of the decay may then reflect the time taken for the excitations to hop and localize between sites on a particular nanoring. Once the carries are localized the recombination is relatively fast likely as a result of the strong coupling with CdSe LO-phonons[51,69,70] and negatively charged selenium rich surface sites (**SI, S9**), hence explaining the relatively overall short lifetime (and low PL quantum yield).

The nanoring PL decay is not uniform across the band, with faster decay on the blue high-energy edge, and with the PL peak maximum shifting to lower energies over ~1 ns. This is again likely a consequence of inhomogeneous broadening within the emission of nanorings, with some energy transfer to nanorings with a smaller band gap following photoexcitation. There could also be energy transfer between different sites of varying thickness (and hence band gap) on the individual nanorings. The low overall

FRET efficiency between nanorings (see **SI, S5**) will further serve to reduce the PL quantum yield. However, the stability of the single nanoring PL precludes transient photoluminescence measurements to fully characterize this and establish whether the low quantum yield for nanorings results from lower yield for all nanorings, or arises because some are emissive and others are quenched. The results are also consistent with the hypothesis that rings which have a higher band energy (bluer PL) undergo faster radiative recombination. From our DFT simulations (Figure 2) it would be expected that these nanorings have a larger radius. Finally, we note in both platelets and nanorings emission from the sub-gap states at 630 nm and 740 nm (see **SI, S10** for spectral slices) are relatively long-lived compared to emission from excitons.

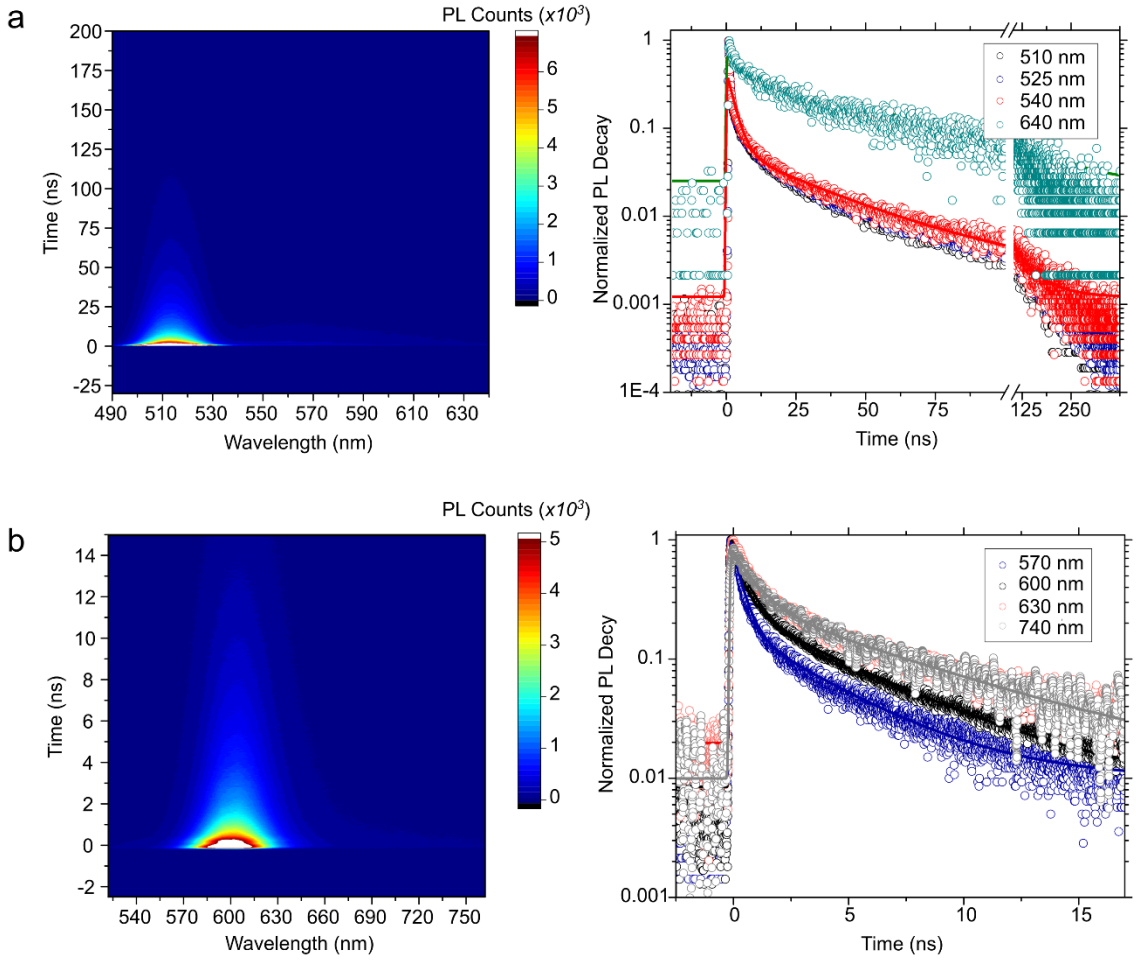

Figure 9: Transient photoluminescence measurements of nanoplatelets and nanorings excited at 405 nm: a. Transient photoluminescence spectrum of 4-monolayer nanoplatelets in solution. There is a multi-exponential decay (right) which decays uniformly across the emission band. At early times the decay is attributed to energy transfer and cooling whereas at later times corresponds to reversible charge trapping. A second, long lived emission feature at ~630 nm is observed. **b.** Transient photoluminescence spectrum of nanorings. The emission is significantly shorter lived than nanoplatlets with a faster decay at higher energies (left). An additional emissive feature ~740 nm is observed which has relatively long lived emission compared with that of excitons and is suggested to originate from sub-band gap defect states.

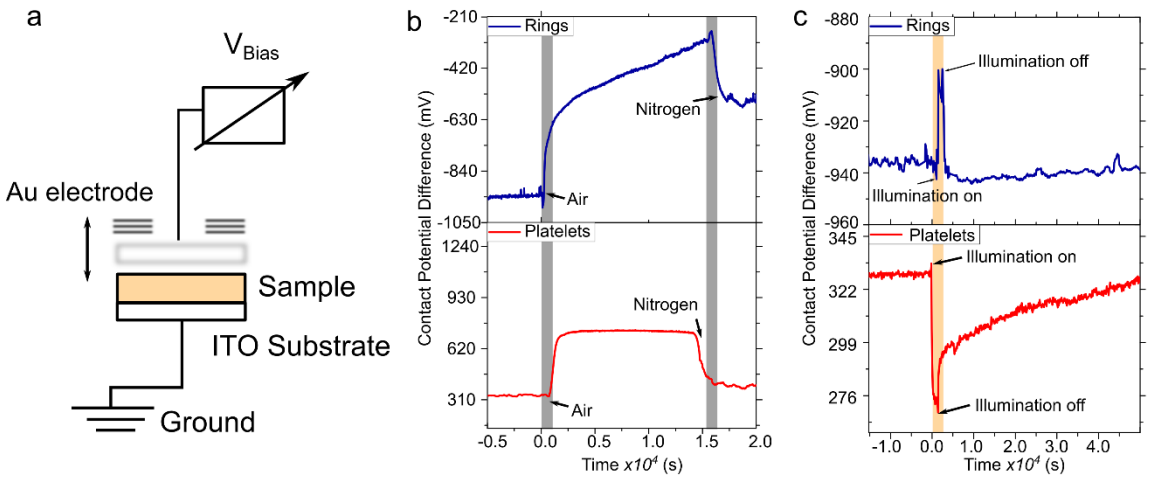

Figure 10: Kelvin probe study of oxygen dependence and surface photovoltage response of nanoplatelets and nanorings. a. Schematic of Kelvin probe setup. In the Kelvin probe contact potential difference (CPD) measurement, a vibrating gold tip (potential V_b) is suspended a distance above a sample on a grounded ITO substrate. The peak-to peak amplitude of the time-varying voltage from the tip is proportional to the sum of V_b and the contact potential difference V_{cpd} between the inner face of the vibrating tip and the sample surface. As V_b is altered to minimise the measured voltage, V_{cpd} can be determined[71]. **b.** The initial dark contact potential difference (CPD) between the stainless steel tip in nitrogen atmosphere is -940 mV and +340 mV for the nanorings and nanoplatelets respectively. In the case of the nanorings and platelets, a rapid increase in work function on the order of 300 mV is observed upon exposure to ambient atmosphere as it is pumped into the system at t=0. This abrupt change is attributed to the formation of a surface dipole as oxygen is absorbed into the active surface of nanomaterials[72]. In the nanorings, the transition into a linear CPD change, between -600 mV to -300 mV, likely represents a further diffusion of oxygen into the rings. At 30 minutes, the atmosphere is replaced with nitrogen and the CPD recovers to -600 mV. This indicates oxygen can be partially removed from physisorbed sites, however the initial binding to oxygen is beyond thermally activated desorption at room temperature. **c.** Surface photovoltage response comparison between rings and platelets in nitrogen. Thin films of samples were held in a dark nitrogen environment then exposed to an AM1.5 white light source for 30 s while the recovery of the CPD is monitored. The magnitude of the SPV response is on the order of 40 mV for both rings and platelets. As, in general, the SPV recovery is trap-dominated we can infer the number and energy depth of trap states depending the CPD change after exposure to white light[72,73]. We find for the rings that the SPV response decays within the instrument time resolution (< 1 s), whereas for the platelets this is a much longer process (> 300 s). This suggests that the traps are deeper and longer lived in the rings compared to platelets.

Finally, to investigate how atmospheric effects and light soaking influence electronic properties in nanorings and nanoplatelets macroscopic Kelvin probe[74] and surface photovoltage (SPV) measurements[71] were performed on thin films of both (Figure 10). The Kelvin probe is sensitive to out of plane charge changes, particularly the net surface dipole *via* measurement of the contact potential difference (CPD; – the difference in work function between sample and tip), hence the orientation, *etc.* of nanostructures on the substrate is also an important consideration. In the case of both nanoplatelets and nanorings we see this is dramatically altered by the introduction of oxygen to the ambient environment (Figure 10a). For nanoplatelets the oxygen alters the contact potential difference (whose

change is proportional to the change in net surface dipole) by ~300 mV and in nanorings by ~600 mV. Interestingly in both nanostructures, after the sudden increase in oxygen concentration, the rate of change in CPD has a biphasic response with an initial fast change and then a slower secondary increase. The initial change in CPD is likely due to incorporation of oxygen *via* electronic bonding. Conversely the second regime likely corresponds to diffusion of surface oxygen, potentially through weak van der Waals interactions. This is supported by the recovery of CPD through the introduction of nitrogen into the system. In nanoplatelets this second phase does not involve a pronounced change in the CPD, with the CPD returning to almost the same value on refilling the chamber with nitrogen; this suggests that oxygen incorporation is much weaker. In addition to the effect of oxygen we also investigated the effect of light exposure on the CPD by measuring the CPD following illumination and extinction. In both materials the CPD changes quite dramatically (~40 mV) on light soaking. In the case of nanoplatelets, the recovery of the CPD is relatively slow as compared to the nanorings. This slow return of the CPD is ascribed to the reduced rate of freeing of charges from trap sites in the nanostructure and suggests that nanoplatelets contain either, a greater number of, or deeper traps[72,75,76]. This is in agreement with the low temperature PL measurements which show that the trap degeneracy (from equation 1) in nanoplatelets is higher than in nanorings, and also confirmed by the slightly lower Urbach energy for nanorings over nanoplatelets. We emphasise that for other measurements in this manuscript (transient absorption, photoluminescence, *etc.*) the samples were encapsulated (films) or sealed (solution) in an inert nitrogen or argon environment.

Conclusion

We have investigated exciton dynamics in colloidal CdSe nanorings. Using ultrasensitive, scatter-free absorption measurements, we have shown forming these rings from nanoplatelets introduces relatively little disorder into the materials. DFT simulations show the changes in the electronic structure lead to a red-shift in the absorption on etching the central hole of the platelets to form a ring. Variation in the size, thickness, and localization properties of the rings leads to a broad absorption and emission with a large Stokes shift as confirmed by single-particle PL measurements. Following photoexcitation, excitons on the nanoring hop between (surface) trap sites before localising, this is in contrast to the delocalized, band-like picture of excitations in nanoplatelets. These increased exciton localization likely emergeds from the localized hole state due to the change in topology and electronic structure from the creation of the nanoring. There is also likely energetic hopping between nanorings of different band energies within the ensemble. The surfaces of nanorings have a large negative charge, suggesting the traps consist of regions of unpassivated selenium. In contrast to nanoplatelets, there is strong coupling between excitons and an LO-phonon mode at 200 cm^{-1}, which we suggest plays a key role in localising excitations. *In-situ* characterization of nanorings during their formation from nanoplatelets suggests this enhanced exciton-phonon coupling is introduced during the etching process. Using low-temperature absorption and emission, we confirm this equilibrium between trap and excitonic emission, with the former dominating at low temperatures.

These results have several implications for the engineering of 2D colloidal nanorings. Firstly, they suggest that passivation of negative selenium traps is key. This might be achieved either *via* appropriate surface ligands or by better removing excess selenium from the etch process. Given exciton-phonon scattering is a major PL loss pathway in these materials, our results additionally suggest that tuning of the material structure is required. This could perhaps be achieved by alloying of the material[77], to reduce coupling with phonon modes and alleviate strain in nanorings, an approach which has had success in some 2D transition metal dichalcogenides[78,79]. In general, the nature of trap states in these materials remains poorly understood and future work should aim to better characterize these, *e.g.*, *via* computational modelling. From a synthetic viewpoint, ensuring all nanorings have the same diameter would lead to emission with narrower linewidths. This could potentially be achieved by flow-synthesis routes[80].

As active materials for quantum dot LEDs, the strong exciton-phonon coupling in nanorings is not advantageous, due to the asymmetry and PL broadening introduced[81]. However, these materials could find use in novel polariton lasers, where the strong exciton-phonon coupling increases the rate of polariton relaxation allowing for low lasing thresholds[82–84]. The fact that the emission is sharp (FWHM μeV range) while at the few-particle level means they could be promising candidates for novel photonic applications which can exploit their toroidal geometry.

For application in solar cells, the high trap density and the fact that the main carriers are excitons as opposed to free charges, limits the use of nanorings, although these materials would be optimal over nanoplatelets. However, if the PL quantum yield can be enhanced, nanorings might find effective use in luminescent solar concentrators, where a high Stokes shift between absorption coupled with the potential for highly directed emission is desirable. In terms of applications that exploit the nanoring shape, our results suggest that surface traps introduced by etching of the platelet center might be a limiting factor[85]. However, our work points to a potentially unusual excitonic fine structure where there is an interplay between effects observed in 2D platelets and 0D dots. Investigating this further with magneto-optical spectroscopies should be the focus of future work.

Acknowledgements

We thank the EPSRC (programme grant: EP/M005143/1) and Winton Program for Physics of Sustainability for financial support. R.H.F. and Y.L. acknowledge support from the Simons Foundation (grant 601946). This work was performed using resources provided by the Cambridge Service for Data Driven Discovery (CSD3) operated by the University of Cambridge Research Computing Service (www.csd3.cam.ac.uk). R.P. thanks Ryan Brady (Cambridge) for assistance with zeta-potential and DLS measurements, Gianluca Grimaldi (Cambridge) for assistance with interpretation of transient absorption data and Juan Climente (Universitat Jaume I, Spain) for insightful discussions. E. R. and S. D. S. acknowledge the European Research Council (ERC) under the European Union's Horizon 2020 research and innovation program (HYPERION, grant agreement number 756962). E. R. was partially supported by an EPSRC Departmental Graduate Studentship. S. D. S. acknowledges funding from the Royal Society and Tata Group (UF150033).

Notes

The raw data underlying this manuscript is freely available at [url to be added in proof].

Supporting Information

TEM images of partially etched nanoplatelets, DFT calculations, temperature dependent X-Ray diffraction measurements, optical pulse compression, analysis of impulsive vibrational spectroscopy and pump-probe data, Raman spectra of partially etched nanorings, temperature dependent absorption and emission spectra, zeta potential measurements

Methods

CdSe Nanorings synthesis

CdSe nanorings (NRs) were synthesized according to the method of Fedin *et al.*[7] following the chemical etching of CdSe nanoplatelets (NPLs) synthesized according to the method of Ithurria *et al.*[2] All materials were purchased from Sigma-Aldrich unless otherwise stated and were used as received. A typical procedure is as follows.

Cadmium myristate was prepared by first reacting myristic acid (1.37 g, 6 mmol) with sodium hydroxide (0.24 g, 6 mmol) in 240 mL methanol. Cadmium nitrate (0.617 g, 2 mmol) dissolved in 40 mL methanol was then added dropwise with vigorous stirring over 1 hour. The white precipitate was collected through vacuum filtration and washed 3 times with 30 mL methanol. The powder was dried under vacuum overnight at 80 °C.

A 50 mL 3-necked flask was loaded with cadmium myristate (170 mg) and 1-octadecene (ODE, 15 mL) then degassed at 100 °C for 10 minutes. The flask was switched to N_2 then cooled to room temperature. Selenium powder (12 mg, 100-mesh) was added under flowing N_2 then the flask degassed at 90 °C for 30 minutes. The flask was switched to N_2 and heated to 140 °C until the Se had fully dissolved. A separate receiving Schlenk flask containing methylcyclohexane (MCH, 10 mL) and degassed oleic acid (OA, 2 mL) in N_2 was prepared. The 3-necked flask was rapidly heated to 240 °C, and finely ground cadmium acetate dihydrate (40 mg, 0.15 mmol) was added to the flask under nitrogen flow when the temperature reached 190 °C. The solution was maintained 240 °C for 4 minutes. The hot solution was then extracted with a glass syringe and metal needle and rapidly injected into the receiving flask. The cloudy solution was allowed to settle for 3 hours then transferred to an Ar glovebox then centrifuged at 12000 g for 5 minutes. The supernatant was discarded and the precipitate was resuspended in 4 mL MCH and filtered through a 0.2 µm PTFE syringe filter. The crude solution was purified twice by precipitation with ethanol, centrifugation and resuspension in MCH. The purified NPLs were stored in MCH.

A quantity of purified nanoplatelets was dispersed into degassed ODE (3 mL) and degassed OAm (1 mL). The absorption spectrum of the NPLs in MCH was used to determine the amount of stock solution to be used. When the sharp absorption feature at 511 nm for a solution of NPLs diluted by a factor of 300 was 0.2 A in a 1 cm cuvette, 1 mL of the undiluted solution was used for the ring etch procedure. The NPL solution in ODE/OAm was transferred to a 25 mL 3-necked flask purged with N_2. The solution was heated to 80 °C under N_2 for 15 minutes to evaporate the MCH then the flask was slowly degassed whilst being allowed to cool to room temperature. Selenium powder (Alfa-Aesar, 7.9 mg, 325-mesh) was dispersed and sonicated in degassed OAm (1 mL) and 0.2 mL of this suspension was added to the degassed NPL solution. The flask was degassed at room temperature for 10 minutes before heating to 140 °C under N_2. The temperature was maintained at 140 °C for 10 minutes, then tri-n-butylphosphine (0.2 ml) was injected into the flask and the temperature was increased to 220 °C. The heating mantle was removed immediately upon reaching 220 °C and the flask was allowed to cool to room temperature. At 37 °C, finely ground cadmium formate (MP Biomedicals, 10 mg) was added to the flask, and the mixture was stirred for 1 hour. The solution was transferred to an Ar glovebox and purified by precipitation with a mixture of ethanol/acetone, centrifugation and resuspension in hexane.

Bright-field Transmission Electron Microscopy

Bright-field transmission electron microscopy was performed with a FEI Tecnai F20 TEM at 200 kV operating voltage. Samples were prepared by deposition of diluted nanocrystals in hexane onto carbon-coated Cu grids (Agar AGS160).

Photoluminescence Quantum Efficiency (PLQE)

Photoluminescence quantum efficiency was performed on a home-built measurement setup consisting of an integrating sphere (Labsphere 4P-GPS-053-SL), collection fibre (Andor SR-OPT8019), spectrograph (Andor Kymera-328i) and detector (Andor iDus 420). The setup was calibrated for spectral sensitivity with a NIST-traceable quartz-tungsten-halogen lamp (Newport 63967-200QC-OA). Excitation was performed with a 520 nm temperature-controlled diode laser (Thorlabs). PLQE values were determined *via* the integrating sphere method[86].

Absorption Spectroscopy

Linear absorption spectra of colloidal nanoplatelets solutions, placed in a 1 mm path length cuvette (Hellma), were measured using a commercial PerkinElmer Lambda 750 UV–vis–NIR setup equipped with a 10 cm integrating sphere module attachment. A Xe lamp was used as an excitation source, and all measurements were performed under standard ambient conditions. In order to collect the scattered light, the sample cuvette was placed on the front window of the sphere. The spectra were measured simultaneously with the solvent hexane to correct for its absorption.

Single particle photoluminescence spectroscopy

The samples were prepared by dropcasting a diluted solution of nanorings (dilution up to 5000 times) onto ~ 5 x 5 mm² glass slides. They were then mounted on the cold finger of a cryostat (Oxford Instrument) allowing the control of the temperature from ≈ 4 K to room temperature. The samples were excited with a continuous wave diode-pumped solid state laser (Thorlabs DJ532) emitting at 533 nm, mounted in its temperature controlled laser mount (Thorlabs TCLDM9). The excitation was focused using a microscope objective (NA = 0.6, spot size ≈ 1 μm). The incident power density was kept around 5 μW/μm². The luminescence was collected using the same optic and spectrally analyzed with an ACTON SP2760i Roper Scientific-Princeton Instruments spectrometer coupled to a nitrogen-cooled SPEC10-2KB-LN (RS-PI) CCD camera (1200 lines per mm grating).

Temperature-Dependent Absorption

An Agilent Cary 6000i UV–vis–NIR spectrophotometer with blank substrate correction was used. Spin-coated samples on fused silica substrates were placed in a continuous-flow cryostat (Oxford Instruments Optistat CF-V) under a helium atmosphere. We allowed the sample temperature to equilibrate for 30 min before taking data.

DFT Calculations

All DFT calculations were performed using the Quantum Espresso suite (v6.4)[87,88]. We used the SG15 norm-conserving pseudopotentials generated by ONCVPSP[89] and the electronic wavefunctions were expanded in a plane wave basis with an energy cutoff of 60 Ry. The exchange correlation functional was approximated by the Perdew-Burke-Ernzerhof (PBE) generalized gradient approximation[90]. A vaccum spacing of 15 Å was added to the supercell in the *z*-dimension to remove any spurious interactions, and atomic positions were relaxed until the residual forces were <0.01 eV/Å. The frequency-dependent dielectric function was computed using the independent particle approximation.

Bulk zincblende CdSe was used to create nanoplatelets with their top and bottom surfaces being the {100} facets, which were passivated by Cl ligands. The nanorings were created in a 3 ×3 supercell, and all structures were stoichiometric in Cd, Se and Cl composition. The Monkhorst-Pack[91] *k*-point sampling scheme used for Brillouin zone has divisions of less than 0.03 $Å^{-1}$, and only the Γ point was sampled in the *z*-direction.

Photothermal Deflection Spectroscopy

PDS measures the refractive index change due to heat that is caused by nonradiative relaxation when the incoming light is absorbed and can be considered a scatter-free technique for measuring absorption capable of measuring 5–6 orders of magnitude weaker absorption than the band-edge absorption. For the measurements, a monochromatic pump light beam produced by a combination of a Light Support MKII 100 W xenon arc source and a CVI DK240 monochromator was shone on the sample (film on Spectrosil fused silica substrate), inclined perpendicular to the plane of the sample, which on absorption produces a thermal gradient near the sample surface via nonradiative relaxation induced heating. This results in a refractive index gradient in the area surrounding the sample surface. This refractive index gradient was further enhanced by immersing the sample in an inert liquid FC-72 Fluorinert (3M Company) that has a high refractive index change per unit change in temperature. A fixed-wavelength CW laser probe beam, produced using a Qioptiq 670 nm fiber-coupled diode laser with temperature stabilizer for reduced beam pointing noise, was passed through this refractive index gradient, producing a deflection proportional to the absorbed light at that particular wavelength, which was detected by a differentially amplified quadrant photodiode and lock-in amplifier (Stanford Research SR830) combination. Scanning through different wavelengths gives the complete absorption spectra.

Kelvin Probe

Kelvin Probe measurements were measured using a RHC Kelvin Probe System (RHC KP030, KP Technology Ltd.), which measured the contact potential difference between the sample surface and a cylindrical gold tip (4 mm diameter). The samples were prepared under dry N_2 conditions and transferred to the environmental chamber containing the Kelvin Probe. The work function (WF) measurement started immediately after the installation, when the samples were conditioned under dry N_2. After stabilization of the work-function signal, indicating reaching the steady-state we began tracking of the WF value. A surface spectroscopy module (AM0.5, SPS020, KP Technology), was used for surface photovoltage (SPV) measurements.

Temperature dependent X-Ray diffraction

XRD was performed using a Bruker X-ray D8 Advance diffractometer with Cu Kα1,2 radiation (λ = 1.541 Å). The Bruker D8 is equipped with Johansson monochromators that eliminate Ka2, AFAIK. Low-temperature measurements were made on cooling between 300 and 12 K using an Oxford Cryosystem PheniX stage (50 K steps; 20 min waited for equilibration of temperature). Spectra were collected with an angular range of $10° < 2\theta < 60°$ and $\Delta\theta = 0.014\,31°$ over 60 min. Measurements were made on drop-casted films from the nanoplatelet or nanoring suspension onto precleaned silicon substrates.

Picosecond Transient Absorption

The picosecond transient absorption (ps-TA) experiments were performed using an Yb-based amplified system (PHAROS, Light Conversion) providing 14.5 W at 1030 nm and 38 kHz repetition rate. The

probe beam is generated by focusing a portion of the fundamental in a 4 mm YAG substrate and spans from 520 to 900 nm. The pump beam is generated by seeding a portion of the fundamental to a narrow band optical parametric oscillator (ORPHEUS-LYRA, Light Conversion). The pump pulse was set to 500 nm. The sample solutions were placed in 1 mm path length cuvettes (Helma). The pump and probe beams were focused to a size of 280 μm × 240 μm and 55 μm × 67 μm, respectively. The pump fluence was typically 30 μJ/cm^2. The white light is delayed using a computer-controlled piezoelectric translation stage (Newport), and a sequence of probe pulses with and without the pump is generated using a chopper wheel (Thorlabs) on the pump beam. The probe pulse transmitted through the sample was detected by a silicon photodiode array camera (Stresing Entwicklungsbüro; visible monochromator 550 nm blazed grating).

Transient Photoluminescence

To record the time-resolved emission scan or photoluminescence decay of the samples, time-correlated single-photon counting (TCSPC) was performed. Samples were excited with a pulsed laser (PicoQuant LDH400 40 MHz) 470 nm, with the resulting photoluminescence decay collected on a 500 mm focal length spectrograph (Princeton Instruments, SpectraPro2500i) with a cooled CCD camera. The instrument response was determined by scattering excitation light into the detector using a piece of frosted glass; a value of 265 ps was obtained.

Femtosecond Transient Absorption Spectroscopy

The fs-TA experiments were performed using an Yb-based amplified system (Pharos, Light Conversion) providing 14.5 W at 1030 nm and a 38 kHz repetition rate. The probe beam was generated by focusing a portion of the fundamental in a 4 mm YAG substrate and spanned from 520 to 1400 nm. The pump beam was generated in a home-built noncollinear optical parametric (NOPAs; 37° cut BBO, type I, 5° external angle) pumped with either the second or third harmonic of the source. The NOPAs output (∼4–5 mW power) was centered at either 520, 660, or 860 nm, and pulses were compressed using a chirped mirror wedge prism (Layterc) combination to a temporal duration of 12 and 17 fs, respectively (upper limit determined by SHG-FROG). The white light was delayed using a computer-controlled piezoelectric translation stage, and a sequence of probe pulses with and without pump was generated using a chopper wheel on the pump beam. The pump irradiance was at 19 μJ/cm^2. After the sample, the probe pulse was split with a 950 nm dichroic mirror (Thor Laboratories). The visible light (520–950 nm) was then imaged with a silicon photodiode array camera (Stresing Entwicklunsbüro; visible monochromator 550 nm blazed grating) with the near-infrared proportion of the probe seeded to an IR monochromator (1200 nm blazed grating) and imaged using an InGaAs photodiode array camera (Sensors Unlimited). This technique allows simultaneous collection of the entire probe spectrum in a single shot. Offsets for the differing spectral response of the detectors was accounted for in the post-processing of data.

Steady-state Raman

Raman measurements were performed with a Renishaw inVia Raman microscope under ambient conditions. Excitation was provided by 532 nm and 633 nm laser lines. The Raman emission was collected by a Leica 100× objective (N.A. = 0.85) and dispersed by a 1800 lines per mm grating. Measurements were performed on thin films of nanoplatelets and nanorings atop a glass microscope slide.

Zeta-potential measurements

Zeta-potential and size distribution measurements were performed on a Malvern Zetasizer NanoZSP, equipped with a 633 nm He-Ne laser with a maximum power of 10mW. A glass cuvette (PCS1115)

was loaded with 400 µl of QDs in hexane (1 mg/ml), and a Malvern Universal Dip Cell (ZEN1002). was used for measurement of zeta-potential**.** All measurements were performed at 25C, with a minimum equilibration period of 2 minutes following sample loading. Zeta-potential distributions were averaged over 5 measurements, each of which consisted of between 50 to 100 runs.

References

(1) Smith, A. M.; Nie, S. Semiconductor Nanocrystals: Structure, Properties, and Band Gap Engineering. *Acc. Chem. Res.* **2010**, *43* (2), 190–200. https://doi.org/10.1021/ar9001069.

(2) Ithurria, S.; Tessier, M. D.; Mahler, B.; Lobo, R. P. S. M.; Dubertret, B.; Efros, A. L. Colloidal Nanoplatelets with Two-Dimensional Electronic Structure. *Nat. Mater.* **2011**, *10* (12), 936–941. https://doi.org/10.1038/nmat3145.

(3) Milliron, D.; Hughes, S. M.; Cui, Y.; Manna, L.; Li, J.; Wang, L. W.; Alivisatos, A. P. Colloidal Nanocrystal Heterostructures with Linear and Branched Topology. *Nature* **2004**, *430* (6996), 190–195. https://doi.org/10.1038/nature02695.

(4) Sigle, D. O.; Zhang, L.; Ithurria, S.; Dubertret, B.; Baumberg, J. J. Ultrathin CdSe in Plasmonic Nanogaps for Enhanced Photocatalytic Water Splitting. *J. Phys. Chem. Lett.* **2015**, *6* (7), 1099–1103. https://doi.org/10.1021/acs.jpclett.5b00279.

(5) Li, Q.; Zhou, B.; McBride, J. R.; Lian, T. Efficient Diffusive Transport of Hot and Cold Excitons in Colloidal Type II CdSe/CdTe Core/Crown Nanoplatelet Heterostructures. *ACS Energy Lett.* **2017**, *2* (1), 174–181. https://doi.org/10.1021/acsenergylett.6b00634.

(6) Rowland, C. E.; Susumu, K.; Stewart, M. H.; Oh, E.; Mäkinen, A. J.; O'Shaughnessy, T. J.; Kushto, G.; Wolak, M. A.; Erickson, J. S.; L. Efros, A.; et al. Electric Field Modulation of Semiconductor Quantum Dot Photoluminescence: Insights into the Design of Robust Voltage-Sensitive Cellular Imaging Probes. *Nano Lett.* **2015**, *15* (10), 6848–6854. https://doi.org/10.1021/acs.nanolett.5b02725.

(7) Fedin, I.; Talapin, D. V. Colloidal CdSe Quantum Rings. *J. Am. Chem. Soc.* **2016**, *138* (31), 9771–9774. https://doi.org/10.1021/jacs.6b05862.

(8) Mitchell, B.; Massey, W. S. Algebraic Topology: An Introduction. *Am. Math. Mon.* **1968**. https://doi.org/10.2307/2313470.

(9) Li, E.; Eggleton, B. J.; Fang, K.; Fan, S. Photonic Aharonov-Bohm Effect in Photon-Phonon Interactions. *Nat. Commun.* **2014**, *5* (3225). https://doi.org/10.1038/ncomms4225.

(10) Chen, P.; Whaley, K. B. Magneto-Optical Response of CdSe Nanostructures. *Phys. Rev. B - Condens. Matter Mater. Phys.* **2004**, *70* (045311). https://doi.org/10.1103/PhysRevB.70.045311.

(11) Becker, M. A.; Vaxenburg, R.; Nedelcu, G.; Sercel, P. C.; Shabaev, A.; Mehl, M. J.; Michopoulos, J. G.; Lambrakos, S. G.; Bernstein, N.; Lyons, J. L.; et al. Bright Triplet Excitons in Caesium Lead Halide Perovskites. *Nature* **2018**, *553* (7687), 189–193.

https://doi.org/10.1038/nature25147.

(12) Simonin, J.; Proetto, C. R.; Pacheco, M.; Barticevic, Z. Electric and Magnetic Field Manipulation and Storage of Charge-Tunable Excitons. *Phys. Rev. B - Condens. Matter Mater. Phys.* **2014**, *89* (075304). https://doi.org/10.1103/PhysRevB.89.075304.

(13) Zipper, E.; Kurpas, M.; Sadowski, J.; Maśka, M. M. Spin Relaxation in Semiconductor Quantum Rings and Dots-a Comparative Study. *J. Phys. Condens. Matter* **2011**, *23* (11), 39–48. https://doi.org/10.1088/0953-8984/23/11/115302.

(14) Ju, S.; Jeong, S.; Kim, Y.; Watekar, P. R.; Han, W. T. Demonstration of All-Optical Fiber Isolator Based on a CdSe Quantum Dots Doped Optical Fiber Operating at 660 Nm. *J. Light. Technol.* **2013**, *31* (16), 3093–3098. https://doi.org/10.1109/JLT.2013.2273215.

(15) Hartmann, N. F.; Otten, M.; Fedin, I.; Talapin, D.; Cygorek, M.; Hawrylak, P.; Korkusinski, M.; Gray, S.; Hartschuh, A.; Ma, X. Uniaxial Transition Dipole Moments in Semiconductor Quantum Rings Caused by Broken Rotational Symmetry. *Nat. Commun.* **2019**, *10* (3253). https://doi.org/10.1038/s41467-019-11225-6.

(16) Kuroda, T.; Mano, T.; Ochiai, T.; Sanguinetti, S.; Sakoda, K.; Kido, G.; Koguchi, N. Optical Transitions in Quantum Ring Complexes. *Phys. Rev. B - Condens. Matter Mater. Phys.* **2005**, *72* (20). https://doi.org/10.1103/PhysRevB.72.205301.

(17) Warburton, R. J.; Schäflein, C.; Haft, D.; Bickel, F.; Lorke, A.; Karrai, K.; Garcia, J. M.; Schoenfeld, W.; Petroff, P. M. Optical Emission from a Charge-Tunable Quantum Ring. *Nature* **2000**, *405*, 926–929. https://doi.org/10.1038/35016030.

(18) Ithurria, S.; Bousquet, G.; Dubertret, B. Continuous Transition from 3D to 1D Confinement Observed during the Formation of CdSe Nanoplatelets. *J. Am. Chem. Soc.* **2011**, *133* (9), 3070–3077. https://doi.org/10.1021/ja110046d.

(19) Diroll, B. T.; Chen, M.; Coropceanu, I.; Williams, K. R.; Talapin, D. V.; Guyot-Sionnest, P.; Schaller, R. D. Polarized Near-Infrared Intersubband Absorptions in CdSe Colloidal Quantum Wells. *Nat. Commun.* **2019**, *10* (4511). https://doi.org/10.1038/s41467-019-12503-z.

(20) Ekimov, A. I.; Hache, F.; Ricard, D.; Flytzanis, C.; Polytechnique, E.; Minchen, T. U. Absorption and Intensity-Dependent Photoluminescence Measurements on CdSe Quantum Dots: Assignment of the First Electronic Transitions. *J. Opt. Soc. Am. B* **1993**, *10* (1), 100–107.

(21) Kim, D.; Kim, D. H.; Lee, J. H.; Grossman, J. C. Impact of Stoichiometry on the Electronic Structure of PbS Quantum Dots. *Phys. Rev. Lett.* **2013**, *110* (19), 1–5.

https://doi.org/10.1103/PhysRevLett.110.196802.

(22) Giansante, C.; Infante, I. Surface Traps in Colloidal Quantum Dots: A Combined Experimental and Theoretical Perspective. *J. Phys. Chem. Lett.* **2017**, *8* (20), 5209–5215. https://doi.org/10.1021/acs.jpclett.7b02193.

(23) Shornikova, E. V.; Golovatenko, A. A.; Yakovlev, D. R.; Rodina, A. V.; Biadala, L.; Qiang, G.; Kuntzmann, A.; Nasilowski, M.; Dubertret, B.; Polovitsyn, A.; et al. Surface Spin Magnetism Controls the Polarized Exciton Emission from CdSe Nanoplatelets. *Nat. Nanotechnol.* **2020**, *1098*. https://doi.org/10.1038/s41565-019-0631-7.

(24) Biadala, L.; Shornikova, E. V.; Rodina, A. V.; Yakovlev, D. R.; Siebers, B.; Aubert, T.; Nasilowski, M.; Hens, Z.; Dubertret, B.; Efros, A. L.; et al. Magnetic Polaron on Dangling-Bond Spins in CdSe Colloidal Nanocrystals. *Nat. Nanotechnol.* **2017**, *12*, 569–57. https://doi.org/10.1038/nnano.2017.22.

(25) Momma, K.; Izumi, F. VESTA: A Three-Dimensional Visualization System for Electronic and Structural Analysis. *J. Appl. Crystallogr.* **2008**, *41*, 653–658. https://doi.org/10.1107/S0021889808012016.

(26) Jackson, W. B.; Amer, N. M.; Boccara, A. C.; Fournier, D. Photothermal Deflection Spectroscopy and Detection. *Appl. Opt.* **1981**, *20* (8), 1333. https://doi.org/10.1364/AO.20.001333.

(27) Tessier, M. D.; Javaux, C.; Maksimovic, I.; Loriette, V.; Dubertret, B. Spectroscopy of Single CdSe Nanoplatelets. *ACS Nano* **2012**, *6* (8), 6751–6758. https://doi.org/10.1021/nn3014855.

(28) Turtos, R. M.; Gundacker, S.; Omelkov, S.; Mahler, B.; Khan, A. H.; Saaring, J.; Meng, Z.; Vasil'ev, A.; Dujardin, C.; Kirm, M.; et al. On the Use of CdSe Scintillating Nanoplatelets as Time Taggers for High-Energy Gamma Detection. *npj 2D Mater. Appl.* **2019**, *3* (37). https://doi.org/10.1038/s41699-019-0120-8.

(29) Greeff, C. W.; Glyde, H. R. Anomalous Urbach Tail in GaAs. *Phys. Rev. B* **1995**, *51* (3), 1778–1783. https://doi.org/10.1103/PhysRevB.51.1778.

(30) Ikhmayies, S. J.; Ahmad-Bitar, R. N. A Study of the Optical Bandgap Energy and Urbach Tail of Spray-Deposited CdS:In Thin Films. *J. Mater. Res. Technol.* **2013**, *2* (3), 221–227. https://doi.org/10.1016/j.jmrt.2013.02.012.

(31) Guyot-Sionnest, P.; Lhuillier, E.; Liu, H. A Mirage Study of CdSe Colloidal Quantum Dot Films, Urbach Tail, and Surface States. *J. Chem. Phys.* **2012**, *137* (15). https://doi.org/10.1063/1.4758318.

(32) Tessier, M. D.; Spinicelli, P.; Dupont, D.; Patriarche, G.; Ithurria, S.; Dubertret, B. Efficient Exciton Concentrators Built from Colloidal Core/Crown CdSe/CdS Semiconductor Nanoplatelets. *Nano Lett.* **2014**, *14* (1), 207–213. https://doi.org/10.1021/nl403746p.

(33) Biadala, L.; Liu, F.; Tessier, M. D.; Yakovlev, D. R.; Dubertret, B.; Bayer, M. Recombination Dynamics of Band Edge Excitons in Quasi-Two-Dimensional Cdse Nanoplatelets. *Nano Lett.* **2014**, *14* (3), 1134–1139. https://doi.org/10.1021/nl403311n.

(34) Klimov, V. I. *Nanocrystal Quantum Dots, Second Edition*; 2017. https://doi.org/10.1201/9781420079272.

(35) Trebino, R.; DeLong, K. W.; Fittinghoff, D. N.; Sweetser, J. N.; Krumbügel, M. A.; Richman, B. A.; Kane, D. J. Measuring Ultrashort Laser Pulses in the Time-Frequency Domain Using Frequency-Resolved Optical Gating. *Rev. Sci. Instrum.* **1997**, *68*, 3277–3295. https://doi.org/10.1063/1.1148286.

(36) Wu, K.; Li, Q.; Jia, Y.; McBride, J. R.; Xie, Z. X.; Lian, T. Efficient and Ultrafast Formation of Long-Lived Charge-Transfer Exciton State in Atomically Thin Cadmium Selenide/Cadmium Telluride Type-II Heteronanosheets. *ACS Nano* **2015**, *9* (1), 961–968. https://doi.org/10.1021/nn506796m.

(37) Wu, K.; Li, Q.; Du, Y.; Chen, Z.; Lian, T. Ultrafast Exciton Quenching by Energy and Electron Transfer in Colloidal CdSe Nanosheet-Pt Heterostructures. *Chem. Sci.* **2015**, *6*, 1049–1054. https://doi.org/10.1039/c4sc02994a.

(38) Kunneman, L. T.; Schins, J. M.; Pedetti, S.; Heuclin, H.; Grozema, F. C.; Houtepen, A. J.; Dubertret, B.; Siebbeles, L. D. A. Nature and Decay Pathways of Photoexcited States in CdSe and CdSe/CdS Nanoplatelets. *Nano Lett.* **2014**. https://doi.org/10.1021/nl503406a.

(39) Li, Q.; Xu, Z.; McBride, J. R.; Lian, T. Low Threshold Multiexciton Optical Gain in Colloidal CdSe/CdTe Core/Crown Type-II Nanoplatelet Heterostructures. *ACS Nano* **2017**, *11* (3), 2545–2553. https://doi.org/10.1021/acsnano.6b08674.

(40) Morgan, D. P.; Maddux, C. J. A.; Kelley, D. F. Transient Absorption Spectroscopy of CdSe Nanoplatelets. *J. Phys. Chem. C* **2018**, *122* (41), 23772–23779. https://doi.org/10.1021/acs.jpcc.8b07733.

(41) Yang, Y.; Ostrowski, D. P.; France, R. M.; Zhu, K.; Van De Lagemaat, J.; Luther, J. M.; Beard, M. C. Observation of a Hot-Phonon Bottleneck in Lead-Iodide Perovskites. *Nat. Photonics* **2016**, *10*, 53–59. https://doi.org/10.1038/nphoton.2015.213.

(42) Price, M. B.; Butkus, J.; Jellicoe, T. C.; Sadhanala, A.; Briane, A.; Halpert, J. E.; Broch, K.;

Hodgkiss, J. M.; Friend, R. H.; Deschler, F. Hot-Carrier Cooling and Photoinduced Refractive Index Changes in Organic-Inorganic Lead Halide Perovskites. *Nat. Commun.* **2015**, *6*, 8420. https://doi.org/10.1038/ncomms9420.

(43) Manser, J. S.; Kamat, P. V. Band Filling with Free Charge Carriers in Organometal Halide Perovskites. *Nat. Photonics* **2014**, *8*, 737–743. https://doi.org/10.1038/nphoton.2014.171.

(44) Geiregat, P.; Houtepen, A.; Justo, Y.; Grozema, F. C.; Van Thourhout, D.; Hens, Z. Coulomb Shifts upon Exciton Addition to Photoexcited PbS Colloidal Quantum Dots. *J. Phys. Chem. C* **2014**, *118*, 22284–22290. https://doi.org/10.1021/jp505530k.

(45) Kambhampati, P. Multiexcitons in Semiconductor Nanocrystals: A Platform for Optoelectronics at High Carrier Concentration. *J. Phys. Chem. Lett.* **2012**, *3*, 1182–1190. https://doi.org/10.1021/jz300239j.

(46) Moroz, P.; Royo Romero, L.; Zamkov, M. Colloidal Semiconductor Nanocrystals in Energy Transfer Reactions. *Chem. Commun.* **2019**, *55*, 3033–3048. https://doi.org/10.1039/c9cc00162j.

(47) De Weerd, C.; Gomez, L.; Zhang, H.; Buma, W. J.; Nedelcu, G.; Kovalenko, M. V.; Gregorkiewicz, T. Energy Transfer between Inorganic Perovskite Nanocrystals. *J. Phys. Chem. C* **2016**, *120* (24), 13310–13315. https://doi.org/10.1021/acs.jpcc.6b04768.

(48) Liebel, M.; Kukura, P. Broad-Band Impulsive Vibrational Spectroscopy of Excited Electronic States in the Time Domain. *J. Phys. Chem. Lett.* **2013**, *4* (8), 1358–1364. https://doi.org/10.1021/jz4004203.

(49) Mooney, J.; Saari, J. I.; Myers Kelley, A.; Krause, M. M.; Walsh, B. R.; Kambhampati, P. Control of Phonons in Semiconductor Nanocrystals via Femtosecond Pulse Chirp-Influenced Wavepacket Dynamics and Polarization. *J. Phys. Chem. B* **2013**, *117* (49), 15651–15658. https://doi.org/10.1021/jp406323f.

(50) Sagar, D. M.; Cooney, R. R.; Sewall, S. L.; Kambhampati, P. State-Resolved Exciton-Phonon Couplings in CdSe Semiconductor Quantum Dots. *J. Phys. Chem. C* **2008**, *112* (25), 9124–9127. https://doi.org/10.1021/jp803386g.

(51) Pandya, R.; Chen, R. Y. S.; Cheminal, A.; Dufour, M.; Richter, J. M.; Thomas, T. H.; Ahmed, S.; Sadhanala, A.; Booker, E. P.; Divitini, G.; et al. Exciton-Phonon Interactions Govern Charge-Transfer-State Dynamics in CdSe/CdTe Two-Dimensional Colloidal Heterostructures. *J. Am. Chem. Soc.* **2018**, *140* (43), 1409–14111. https://doi.org/10.1021/jacs.8b05842.

(52) Maddux, C. J. A.; Kelley, D. F.; Kelley, A. M. Weak Exciton-Phonon Coupling in CdSe

Nanoplatelets from Quantitative Resonance Raman Intensity Analysis. *J. Phys. Chem. C* **2018**, *122* (47), 27100–27106. https://doi.org/10.1021/acs.jpcc.8b10125.

(53) Lin, C.; Kelley, D. F.; Rico, M.; Kelley, A. M. The "Surface Optical" Phonon in CdSe Nanocrystals. *ACS Nano* **2014**, *8* (4), 3928–3938. https://doi.org/10.1021/nn5008513.

(54) Mork, A. J.; Lee, E. M. Y.; Tisdale, W. A. Temperature Dependence of Acoustic Vibrations of CdSe and CdSe-CdS Core-Shell Nanocrystals Measured by Low-Frequency Raman Spectroscopy. *Phys. Chem. Chem. Phys.* **2016**, *18*, 28797–28801. https://doi.org/10.1039/c6cp05683k.

(55) Dzhagan, V. M.; Valakh, M. Y.; Milekhin, A. G.; Yeryukov, N. A.; Zahn, D. R. T.; Cassette, E.; Pons, T.; Dubertret, B. Raman-and IR-Active Phonons in CdSe/CdS Core/Shell Nanocrystals in the Presence of Interface Alloying and Strain. *J. Phys. Chem. C* **2013**, *117* (35), 18225–18233. https://doi.org/10.1021/jp4046808.

(56) Brumberg, A.; Harvey, S. M.; Philbin, J. P.; Diroll, B. T.; Lee, B.; Crooker, S. A.; Wasielewski, M. R.; Rabani, E.; Schaller, R. D. Determination of the In-Plane Exciton Radius in 2D CdSe Nanoplatelets via Magneto-Optical Spectroscopy. *ACS Nano* **2019**, *13* (8), 8589–8596. https://doi.org/10.1021/acsnano.9b02008.

(57) Zhang, Y.; Mascarenhas, A. Scaling of Exciton Binding Energy and Virial Theorem in Semiconductor Quantum Wells and Wires. *Phys. Rev. B - Condens. Matter Mater. Phys.* **1999**, *59* (2040). https://doi.org/10.1103/PhysRevB.59.2040.

(58) Achtstein, A. W.; Schliwa, A.; Prudnikau, A.; Hardzei, M.; Artemyev, M. V.; Thomsen, C.; Woggon, U. Electronic Structure and Exciton-Phonon Interaction in Two-Dimensional Colloidal Cdse Nanosheets. *Nano Lett.* **2012**, *12* (6), 3151–3157. https://doi.org/10.1021/nl301071n.

(59) Benchamekh, R.; Gippius, N. A.; Even, J.; Nestoklon, M. O.; Jancu, J. M.; Ithurria, S.; Dubertret, B.; Efros, A. L.; Voisin, P. Tight-Binding Calculations of Image-Charge Effects in Colloidal Nanoscale Platelets of CdSe. *Phys. Rev. B - Condens. Matter Mater. Phys.* **2014**, *89*, 035307. https://doi.org/10.1103/PhysRevB.89.035307.

(60) García-Santamaría, F.; Chen, Y.; Vela, J.; Schaller, R. D.; Hollingsworth, J. A.; Klimov, V. I. Suppressed Auger Recombination in "Giant" Nanocrystals Boosts Optical Gain Performance. *Nano Lett.* **2009**, *9* (10), 3482–3488. https://doi.org/10.1021/nl901681d.

(61) Hou, X.; Kang, J.; Qin, H.; Chen, X.; Ma, J.; Zhou, J.; Chen, L.; Wang, L.; Wang, L. W.; Peng, X. Engineering Auger Recombination in Colloidal Quantum Dots via Dielectric Screening. *Nat. Commun.* **2019**, *10*, 1750. https://doi.org/10.1038/s41467-019-09737-2.

(62) Wang, L.; Chen, Z.; Liang, G.; Li, Y.; Lai, R.; Ding, T.; Wu, K. Observation of a Phonon Bottleneck in Copper-Doped Colloidal Quantum Dots. *Nat. Commun.* **2019**, *10*, 4532. https://doi.org/10.1038/s41467-019-12558-y.

(63) Biadala, L.; Liu, F.; Tessier, M. D.; Yakovlev, D. R.; Dubertret, B.; Bayer, M. Recombination Dynamics of Band Edge Excitons in Quasi-Two-Dimensional Cdse Nanoplatelets. *Nano Lett.* **2014**, *14* (3), 1134–1139. https://doi.org/10.1021/nl403311n.

(64) Cho, W.; Kim, S.; Coropceanu, I.; Srivastava, V.; Diroll, B. T.; Hazarika, A.; Fedin, I.; Galli, G.; Schaller, R. D.; Talapin, D. V. Direct Synthesis of Six-Monolayer (1.9 Nm) Thick Zinc-Blende CdSe Nanoplatelets Emitting at 585 Nm. *Chem. Mater.* **2018**, *30*, 6957–6960. https://doi.org/10.1021/acs.chemmater.8b02489.

(65) Gao, J.; Zhang, J.; Van De Lagemaat, J.; Johnson, J. C.; Beard, M. C. Charge Generation in PbS Quantum Dot Solar Cells Characterized by Temperature-Dependent Steady-State Photoluminescence. *ACS Nano* **2014**, *8* (12), 12814–12825. https://doi.org/10.1021/nn506075s.

(66) Zhang, J.; Tolentino, J.; Smith, E. R.; Zhang, J.; Beard, M. C.; Nozik, A. J.; Law, M.; Johnson, J. C. Carrier Transport in PbS and PbSe QD Films Measured by Photoluminescence Quenching. *J. Phys. Chem. C* **2014**, *118* (29), 16228–16235. https://doi.org/10.1021/jp504240u.

(67) Gilmore, R. H.; Liu, Y.; Shcherbakov-Wu, W.; Dahod, N. S.; Lee, E. M. Y.; Weidman, M. C.; Li, H.; Jean, J.; Bulović, V.; Willard, A. P.; et al. Epitaxial Dimers and Auger-Assisted Detrapping in PbS Quantum Dot Solids. *Matter* **2019**, *1* (1), 250–265. https://doi.org/10.1016/j.matt.2019.05.015.

(68) Rabouw, F. T.; Van Der Bok, J. C.; Spinicelli, P.; Mahler, B.; Nasilowski, M.; Pedetti, S.; Dubertret, B.; Vanmaekelbergh, D. Temporary Charge Carrier Separation Dominates the Photoluminescence Decay Dynamics of Colloidal CdSe Nanoplatelets. *Nano Lett.* **2016**, *16* (3), 2047–2053. https://doi.org/10.1021/acs.nanolett.6b00053.

(69) Lin, C.; Gong, K.; Kelley, D. F.; Kelley, A. M. Size Dependent Exciton Phonon Coupling in CdSe Nanocrystals through Resonance Raman Excitation Profile Analysis. *J. Phys. Chem. C* **2015**, *119* (13), 7491–7498. https://doi.org/10.1021/acs.jpcc.5b00774.

(70) Morello, G.; De Giorgi, M.; Kudera, S.; Manna, L.; Cingolani, R.; Anni, M. Temperature and Size Dependence of Nonradiative Relaxation and Exciton-Phonon Coupling in Colloidal CdTe Quantum Dots. *J. Phys. Chem. C* **2007**, *111* (16), 5846–5849. https://doi.org/10.1021/jp068307t.

(71) Baikie, I. D.; Mackenzie, S.; Estrup, P. J. Z.; Meyer, J. A. Noise and the Kelvin Method. *Rev. Sci. Instrum.* **1991**, *62*, 1326. https://doi.org/10.1063/1.1142494.

(72) Szemjonov, A.; Galkowski, K.; Anaya, M.; Andaji-Garmaroudi, Z.; Baikie, T. K.; Mackowski, S.; Baikie, I. D.; Stranks, S. D.; Islam, M. S. Impact of Oxygen on the Electronic Structure of Triple-Cation Halide Perovskites. *ACS Mater. Lett.* **2019**, *1* (5), 506–510. https://doi.org/10.1021/acsmaterialslett.9b00294.

(73) Nonnenmacher, M.; O'Boyle, M. P.; Wickramasinghe, H. K. Kelvin Probe Force Microscopy. *Appl. Phys. Lett.* **1991**, *58* (2921). https://doi.org/10.1063/1.105227.

(74) Zisman, W. A. A New Method of Measuring Contact Potential Differences in Metals. *Rev. Sci. Instrum.* **1932**, *3* (367). https://doi.org/10.1063/1.1748947.

(75) Sadewasser, S.; Glatzel, T.; Rusu, M.; Jäger-Waldau, A.; Lux-Steiner, M. C. High-Resolution Work Function Imaging of Single Grains of Semiconductor Surfaces. *Appl. Phys. Lett.* **2002**, *80* (2979). https://doi.org/10.1063/1.1471375.

(76) Jaramillo-Quintero, O. A.; Triana, M. A.; Rincon, M. E. Optimization of Charge Transfer and Transport Processes at the CdSe Quantum Dots/TiO2 Nanorod Interface by TiO2 Interlayer Passivation. *J. Phys. D. Appl. Phys.* **2017**, *50* (23). https://doi.org/10.1088/1361-6463/aa6e7c.

(77) Kelestemur, Y.; Guzelturk, B.; Erdem, O.; Olutas, M.; Erdem, T.; Usanmaz, C. F.; Gungor, K.; Demir, H. V. CdSe/CdSe1-XTexCore/Crown Heteronanoplatelets: Tuning the Excitonic Properties without Changing the Thickness. *J. Phys. Chem. C* **2017**, *121* (8), 4650–4658. https://doi.org/10.1021/acs.jpcc.6b11809.

(78) Niehues, I.; Schmidt, R.; Drüppel, M.; Marauhn, P.; Christiansen, D.; Selig, M.; Berghäuser, G.; Wigger, D.; Schneider, R.; Braasch, L.; et al. Strain Control of Exciton–Phonon Coupling in Atomically Thin Semiconductors. *Nano Lett.* **2018**, *18* (3), 1751–1757.

(79) Smith, A. M.; Mohs, A. M.; Nie, S. Tuning the Optical and Electronic Properties of Colloidal Nanocrystals by Lattice Strain. *Nat. Nanotechnol.* **2009**, *4* (1), 56–63. https://doi.org/10.1038/nnano.2008.360.

(80) Naughton, M. S.; Kumar, V.; Bonita, Y.; Deshpande, K.; Kenis, P. J. A. High Temperature Continuous Flow Synthesis of CdSe/CdS/ZnS, CdS/ZnS, and CdSeS/ZnS Nanocrystals. *Nanoscale* **2015**, *7*, 15895–15903. https://doi.org/10.1039/c5nr04510j.

(81) Bae, W. K.; Lim, J.; Lee, D.; Park, M.; Lee, H.; Kwak, J.; Char, K.; Lee, C.; Lee, S. R/G/B/Natural White Light Thin Colloidal Quantum Dot-Based Light-Emitting Devices. *Adv. Mater.* **2014**, *26*, 6387–6393. https://doi.org/10.1002/adma.201400139.

(82) Orosz, L.; Réveret, F.; Médard, F.; Disseix, P.; Leymarie, J.; Mihailovic, M.; Solnyshkov, D.; Malpuech, G.; Zuniga-Pérez, J.; Semond, F.; et al. LO-Phonon-Assisted Polariton Lasing in a ZnO-Based Microcavity. *Phys. Rev. B - Condens. Matter Mater. Phys.* **2012**, *85* (12). https://doi.org/10.1103/PhysRevB.85.121201.

(83) Maragkou, M.; Grundy, A. J. D.; Ostatnick, T.; Lagoudakis, P. G. Longitudinal Optical Phonon Assisted Polariton Laser. *Appl. Phys. Lett.* **2010**, *97* (11). https://doi.org/10.1063/1.3488012.

(84) Dang, C.; Lee, J.; Breen, C.; Steckel, J. S.; Coe-Sullivan, S.; Nurmikko, A. Red, Green and Blue Lasing Enabled by Single-Exciton Gain in Colloidal Quantum Dot Films. *Nat. Nanotechnol.* **2012**, *7* (5), 335–339. https://doi.org/10.1038/nnano.2012.61.

(85) Meinardi, F.; Colombo, A.; Velizhanin, K. A.; Simonutti, R.; Lorenzon, M.; Beverina, L.; Viswanatha, R.; Klimov, V. I.; Brovelli, S. Large-Area Luminescent Solar Concentrators Based on Stokes-Shift-Engineered Nanocrystals in a Mass-Polymerized PMMA Matrix. *Nat. Photonics* **2014**, *8*, 392–399. https://doi.org/10.1038/nphoton.2014.54.

(86) de Mello, J. C.; Wittmannn, H. F.; Friend, R. H. An Improved Experimental Determination of External Photoluminescence Quantum Efficiency. *Adv. Mater.* **1997**, *9* (3), 230. https://doi.org/10.1002/adma.200903328.

(87) Giannozzi, P.; Baroni, S.; Bonini, N.; Calandra, M.; Car, R.; Cavazzoni, C.; Ceresoli, D.; Chiarotti, G. L.; Cococcioni, M.; Dabo, I.; et al. QUANTUM ESPRESSO: A Modular and Open-Source Software Project for Quantum Simulations of Materials. *J. Phys. Condens. Matter* **2009**, *21* (39), 395502. https://doi.org/10.1088/0953-8984/21/39/395502.

(88) Giannozzi, P.; Andreussi, O.; Brumme, T.; Bunau, O.; Nardelli, Buongiorno, M.; Calandra, M.; Car, R.; Cavazzoni, C.; Ceresoli, D.; Cococcioni, M.; et al. Advanced Capabilities for Materials Modelling with Quantum ESPRESSO. *J. Phys. Condens. Matter* **2017**, *29*, 465901.

(89) Hamann, D. R. Optimized Norm-Conserving Vanderbilt Pseudopotentials. *Phys. Rev. B - Condens. Matter Mater. Phys.* **2013**, *88* (8), 1–10. https://doi.org/10.1103/PhysRevB.88.085117.

(90) Perdew, J. P.; Burke, K.; Ernzerhof, M. Generalized Gradient Approximation Made Simple. *Phys. Rev. Lett.* **1996**, *77*, 3865–3868. https://doi.org/10.1103/PhysRevLett.77.3865.

(91) Pack, J. D.; Monkhorst, H. J. Special Points for Brillouin-Zone Integrations. *Phys. Rev. B* **1976**, *13*, 5188. https://doi.org/10.1103/PhysRevB.16.1748.

For table of contents only